# Co-effect of microstructure and surface constraints on plastic deformation in micro- and meso-scaled forming process

M.Y. Mao[a, b], L.F. Peng[a*], M.W. Fu[b#], X.M. Lai[a]

[a:] State Key Laboratory of Mechanical System and Vibration, Shanghai Jiao Tong University, Shanghai 200240, People's Republic of China

[b:] Department of Mechanical Engineering, The Hong Kong Polytechnic University, Hung Hom, Kowloon, Hong Kong

*Tel.: +8602134206303. E-mail address: penglinfa@sjtu.edu.cn (L.F. Peng).

#Tel.: +85227665527. E-mail address: mmmwfu@polyu.edu.hk (M.W. Fu).

## Abstract

The plastic deformation of materials is affected by external boundaries and microstructures, both of which can induce a serious phenomenon, viz., "size effects" in mircroforming process. The interaction of these two kinds of size effects, however, is still not clear, thus significantly obstacles the understanding and development of microforming process. In this study, the co-effect of microstructure and surface constraints on the plastic deformation of material was investigated by using the barreling compression tests (BCT) of micro- and meso- scaled cylindrical pure copper specimens. Through comparing the barreling degree and the distribution of deformation bands of compressed specimens in different size scales, a size effect on plastic deformation caused by the interaction of microstructure and surface constraints was observed. To determine the mechanism of the observed size effect, an extended upper bound solution of barreling was firstly developed by employing surface layer theory and validated by comparing the predicted average and scatter values of barreling magnitude with the experimental measurements in different size scales. Based on the validated solution, the energies dissipated by inter-grain restrictions and surface constraints in the deformation of different scaled specimens were obtained and compared, and the mechanism of size effect on plastic deformation was determined as the change of dominating restrictions to grain rotation from inter-grain restriction to surface constraints. Furthermore, the critical size scale point for the transformation of dominating restrictions as well as the dependence of the critical size scale point on the shape of

specimen and surface friction was obtained. The research thus provides an in-depth understanding of the plastic deformation in micro- and meso-scaled deformation and thus facilitates the forming of the desired geometry and shape and achieving of the tailored quality of the micro- and meso-scaled deformed parts.

**Keywords:** Surface constraints, Inter-grain restrictions, Size effect, Micro-scaled deformation, Meso-scaled deformation

**Nomenclatures**

| | |
|---|---|
| $A_i$ | Area of section i |
| b | Barreling parameter |
| $b_{opt}$ | Optimized barreling parameter |
| d | Average grain size |
| $D_1$, $D_2$, $D_3$ | Size dependent parameters |
| $D_{cb}$ | Diameter of the bottom contact surface |
| $D_{cu}$ | Diameter of the upper contact surface |
| $D_m$ | Diameter of the middle plane |
| f | Friction factor |
| H | Initial height of workpiece |
| $H_i$ | Height of section i |
| $H_r$ | The obtained height after compression |
| J | The dissipated energy |
| K | Shear stress of material |

| | |
|---|---|
| $K_i$ | Shear stress of the inner grains |
| $K_s$ | Shear stress of the surface grains |
| $L_s$ | Slip length |
| m | Orientation factor of single crystals |
| M | Tayler factor |
| $p_{ave}$ | Average forging pressure |
| R | Initial radius of workpiece |
| $r_e$ | Height reduction in compression |
| $R_i$ | Equivalent radius of section i |
| $R_r$ | The average radius of workpiece after compression |
| Rre | Shares of the dissipated energy by external restriction |
| Rri | Shares of the dissipated energy by inter-grain restriction |
| $S_0$ | The initial area of interface |
| $S_i$ | Area of the interface of the inner grains |
| $S^s$ | Area of the interface of the surface grains |
| $\dot{u}$ | Punch velocity |
| $\dot{w}_f$ | Frictional dissipation |
| $\dot{w}_{Ii}$ | Strain energy dissipation of the inner grains |
| $\dot{w}_{Is}$ | Strain energy dissipation of the surface grains |
| $\dot{w}_r$ | Dissipated energy caused by restrictions |
| $\dot{w}_{re}$ | Dissipated energy caused by surface constraints |
| $\dot{w}_{ri}$ | Dissipated energy caused by inter-grain restrictions |

| | |
|---|---|
| $\Delta R$ | The difference between the maximum and the top radii |
| $\varepsilon_{yi}$ | Y-axial strain of the inner grains |
| $\varepsilon_{ys}$ | Y-axial strain of the surface grains |
| $\eta$ | Scale factor |
| $\eta_s$ | Proportion of the surface grains |
| $\sigma$ | Flow stress of material |
| $\sigma^i$ | Flow stress of the inner grains |
| $\sigma^s$ | Flow stress of the surface grains |
| $\tau_R$ | Micro-scaled shear stress |
| $\tau_s$ | Friction stress on the contacting surface |
| $\varphi$ | Barreling shape parameter |

## 1 Introduction

Due to the overwhelming trend of product miniaturization in many industrial clusters, micro-manufacturing technologies such as micromachining, micro laser machining and LIGA technology, etc., have been widely studied and well developed. Microforming is one of the most attractive approaches to fabricating micro-parts for its unique advantages such as high productivity, low cost and the good mechanical properties of microformed parts [1-4]. Compared with other fabricating methods, the accuracy in dimension and geometry of microformed part is still not competitive, since with a significant reduction of specimen size, the process parameters are significantly affected by the "size effect", and the conventional knowledges are no longer applicable in micro- and meso-scaled forming process[5].

The so called "size effect" in metal forming process refers to the variation of deformation behaviors including material flow, fracture, friction, springback, etc. induced by the scaling of

specimen size, the change of microstructure grain size, etc. Attentions have been paid to this field for a few decades and conclusions such as the flow stress and fracture strain of material decreases with the specimen size at the micro-scale of metal working[1], and surface irregularity increases with scaling down of size [6]. Generally, the reason of size effect in metal forming process is the size of some intrinsic structures does not decrease with specimen size, and with the scaling down of specimen size, the behaviors of these intrinsic characters become more dominating [3].

The best known size effect in polycrystalline metals is caused by microstructures such as grains. Since the size of grain is not decreased with the scaling of specimen size, the behavior of individual grains becomes more and more important in influencing the overall behavior of material [7]. The ratio of grain size to specimen or feature size, $d_G/d$, is usually proposed as the scale factor, because with the increase of the ratio from a very small number to 1, any state from polycrystal to single crystal can be represented [5]. The flow stress of material is found to be significantly dependent on $d_G/d$. With the increase of $d_G/d$ from 0 to 1, the average flow stress of material in uniaxial tension tests is reported to decrease. The physical mechanism of the size effect is considered to be the difference in the restrictions to surface and inner grains [8-12]. Inner grains are restricted by neighbor grains, while surface grains have free surfaces which are not restricted by neighbor grains. Thus the deformation of surface grains is easier than inner grains, indicating a lower resistance to the deformation in surface grains than in inner grains. With the increase of $d_G/d$, the share of surface grains in the tensile specimen increases, which leads to the descending of the measured flow stress. Another property of material affected by microstructural size effect is fracture. The variation of fracture strain with $d_G/d$ was studied using uniaxial tensile tests, and it was found the fracture strain decreases rapidly with the increase of

$d_G/d$. From SEM fractography, it can be seen that the amount of microvoids seen at the fracture region decreases with the increase of $d_G/d$ [13, 14]. The physical mechanism of microstructural size effect on fracture strain is still not so clear. Some researchers attributed it to the difference in the restrictions to surface and inner grains. As the surface grains are less restricted, the stress state is more close to plane stress condition than inner grains. The difference in stress condition leads to different processes of void nucleation, growth and coalescence in surface and inner grains. Then the increasing share of surface grains can lead to the variation of fracture strain [15]. Some other researchers took the crystalline anisotropy as the mechanism of microstructural size effect on fracture behavior. With the increase of $d_G/d$, the influence of crystalline anisotropy of individual grains becomes more significant, which could cause strain localization and speed up the fracture [16]. In addition, the increasing influence of crystalline anisotropy can cause the increase of the scatter of the measured flow stress and fracture strain as well as the surface irregularity with $d_G/d$ [17, 18].

Another widely discussed size effect to explain the strengthening of metals in small scales is “gradient effect”. Keeping all geometrical proportions identical, downscaling the geometry of workpiece will naturally lead to an increase of strain gradient in some deformation scenarios such as micro-bending [19]. The gradient has to be accommodated geometrically in the lattice by curvature, which is intrinsically limited through the lattice structure. To accommodate the curvatures, extra geometrically necessary dislocations (GND) must be introduced to lattice, which obstruct plastic slip and contribute to additional hardening [20]. Experimental observation of this kind of size effect can be found in the processes, such as micro torsion [21], micro- and nano-indentations [22] and micro bending [23], in which different deformation modes such as tension, compression and shear co-exist.

Besides the microstructures and strain gradient, the interaction of the carriers of plastic slip with the external boundaries or with interfaces with a different material can also induce size effect [20]. The physical condition at the boundary or interface may either restrict or freely facilitate the deformation nearby the boundary. For polycrystalline metals, plastic slip is carried by dislocations which can either be blocked at the boundary (constrained) or glide out of it (unconstrained), leaving behind a surface step. As the external constraints are applied to the boundary of materials and the influence of the boundary layer generally covers a certain volume, which explains the importance of the surface-to-volume ratio as found in experimental analyses [24]. In the case of small, thin or multi-layered structures, all materials are relatively close to the physical boundary or interface. These size effects therefore naturally induce the dimensional constraint [25].

However, the study of individual size effect is not enough for the prediction of plastic deformation in microforming process, since in most of the real forming process, different kinds of size effects take effects simultaneously, and the interactions of different size effect should be considered. A typical example of the co-effect of different kinds of size effects is springback angle in microbending process. Experimental results reveal that for the small thickness ratios, the springback angle increases with the decreasing t/d ratio, however, when the thickness ratio becomes larger, the springback angle increases with increasing sheet thickness [26, 27]. According to the microstructural size effect, the increasing surface grains can cause a reduction in the springback angle; however, the increasing strain gradient effect can cause an increase in springback angle [28]. Hence, the variation of sprinback angle with the decrease of t/d ratio can be regarded as the co-effect of strain gradient and microstructure size. For small thickness ratios,

the microstructural size effect is dominant, and for large thickness ratios, strain gradient effect becomes dominant [3].

Similarly, the co-effect of microstructure and surface constraint can also be imagined. As surface constraint is applied to the surface grains thus the surface grains are more restricted than inner grains. However, according to the theory of microstructural size effect, the surface grains are less restricted, because there are less neighbor grains around the surface grains. Both of restrictions are unavoidable in miroforming process, but how the grains behave with these two kinds of restriction is not able to be predicted by either of the size effects. Till now seldom study can shed lights to the co-effect of these two kinds of size effects, which significantly obstacles the application of microforming process in the industry. This study tries to be the pioneer work to determine the co-effect of different size effects. In order to focus on the co-effect of microstructures and surface constraints, the barreling compression tests (BCT) of cylinder pure copper specimens were conducted, due to the relatively simple strain distribution in BCT and the influence of strain gradient can be neglected. More importantly, barreling is defined as the heterogeneous deformation caused by interfacial friction in compression process, which reflects the volume and strain distribution of the compressed parts and effect of surface friction on overall plastic deformation [29].

The barreling phenomenon in conventional scale is well studied experimentally [30-33] and theoretically [34-43]. In micro- and meso- forming process, on the other hand, the studies on barreling are not as comprehensive as in conventional scale due to the more irregular barreling shape of the small scaled specimens [12, 17, 44]. The irregularity or the inhomogeneous deformation observed in micro- and meso-scaled compressed specimen is caused by the anisotropy of individual grains. With the decrease of specimen size and the increase of grain size,

the number of grains across the section of specimen decreases, and the deformation behavior of every single grain plays a more important role in the overall deformation. Such a size effect is also reflected in the measured flow stress since the increase of grain size and the decrease of specimen size increases the scatter of flow stress [18]. From the view of definition, however, the irregularity in the shape of compressed specimen is not a part of barreling as the magnitude of irregularity is not affected by interfacial friction. The final shape of compressed specimen is thus constructed by barreling and irregularity. In macro scale, the irregularity is not so significant and the specimen shape is approximately the barreling shape, thus the degree of barreling can be obtained directly by measurement of the shape of side wall. With the decrease of specimen size, irregularity gets more significant, and there is a bigger difference between the barreling shape and the real shape of the side wall.

To explore the barreling phenomenon in micro- and meso-scaled deformation, the effect of grain anisotropy on the final shape of specimen should be treated carefully. The most common way to deal with the problem is crystal plasticity finite element (CPFE) method. By using CPFE Method, the phenomenon caused such as the anisotropy in yielding and hardening [45], the surface roughening [46], and the earing [47] in deformation process are well studied. The general procedure of CPFE method to simulate the forming process includes firstly modeling the grain size and orientation distribution in the workpiece, secondly, applying the crystal plasticity constitutive relation to the grains, and then by taking advantage of finite element method, calculating the deformation of workpiece [48]. As the crystal plasticity constitutive model is derived based on the generation and slip of dislocations, CPFE method can be used to analyze the micro mechanisms of deformation. But the general relations of parameters such as scale factor and surface friction with the deformation degree is hard to obtain by using the method.

In this study, micro- and meso- scaled BCT was conducted to study the co-effect of microstructure and surface constraints on plastic deformation. To deal with the effect of grain anisotropy, a new method of calculating the barreling shape was particularly proposed. The physical phenomenon of co- effect was obtained by comparing the barreling shape of the samples with different grain and geometry sizes. An analytical model of barreling was established based on the upper bound method and was validated with the physical experiments. Based on the model, the energies dissipated by inter-grain restriction and surface constraints were calculated and compared to reveal the mechanism of co-effect on plastic deformation. The study provides an in-depth understanding of the effect of interfacial friction on the overall deformation of material and its evolution with size scale, which helps improving the efficiency of microforming process and the accuracy of microformed parts.

## 2 Research methodology

The research methodology is proposed and presented in Fig. 1.

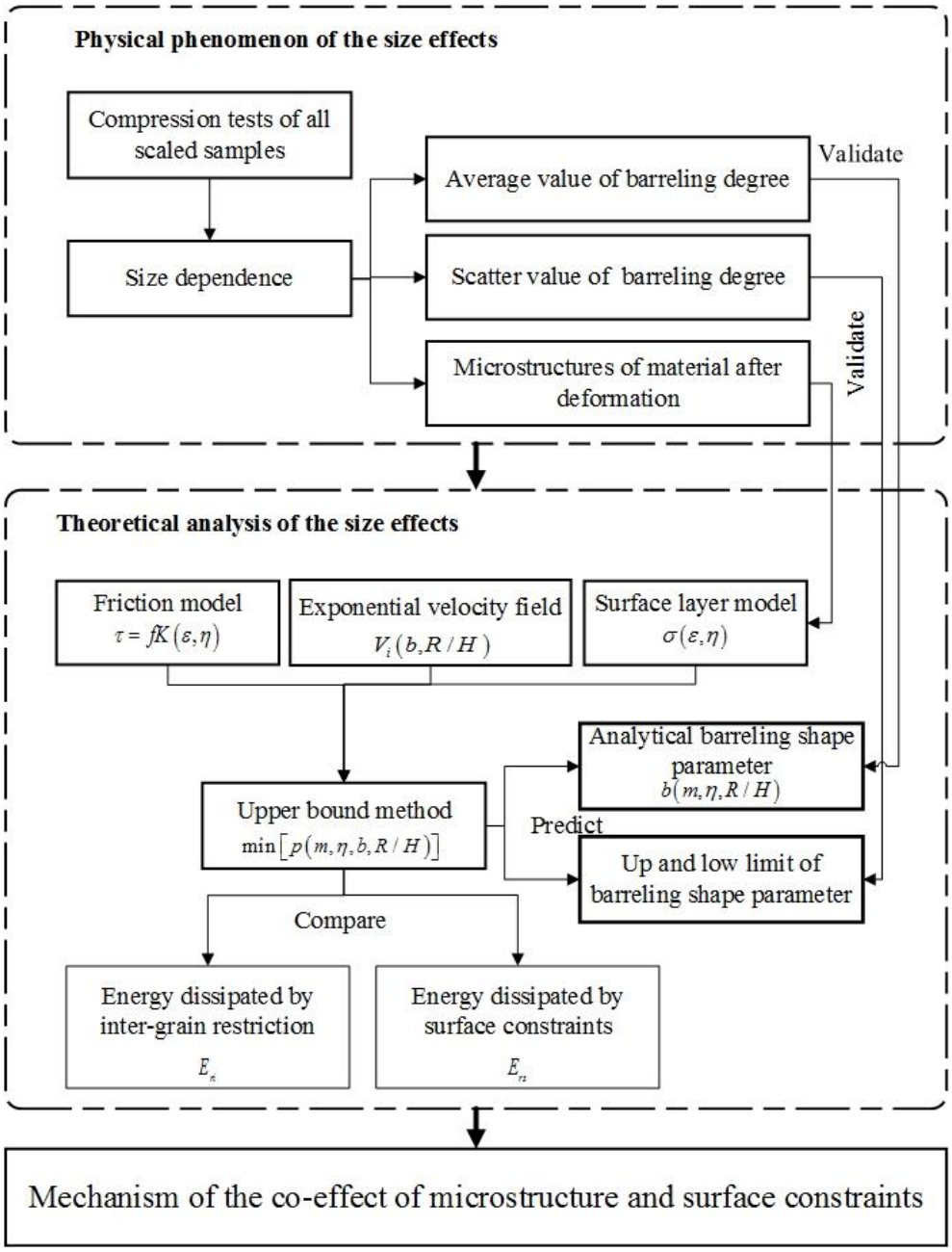


**Fig. 1.** Methodology for study of the co-size effect of microstructure and surface constraints

Barreling compression tests of cylindrical pure copper specimens from meso- to micro-scales with different grain sizes were conducted. The profiles of the compressed specimens were scanned and the distribution of deformation bands in different scaled specimens were observed

to determine the phenomenon of size effect. To reveal the effect of inter-grain restrictions and surface constraints on the plastic deformation, an extended up bound solution was firstly established by employing surface layer constitutive model and velocity field proposed by Avitzur et al. [38], and then validated by comparing the predicted barreling parameter with the experimental measurements. In tandem with the validated up bound solution, the deformation energy dissipated by inter-grain restrictions and surface constraints in compression processes from micro-scale to meso-scale were obtained respectively. And a theoretical analysis of the mechanisms for the size effect on plastic deformation is conducted based on the dissipated energies. Finally, the co-size effect of microstructure and surface constraints was concluded, according to the theoretical analysis.

## 3 Experiments and results

### 3.1 Experimental setup

In this study, a series of barreling compression tests using the cylindrical specimens with different dimensions and grain sizes were conducted in dry friction condition. The experiment process includes three steps, viz., specimen preparation, compression test and measuring barreling profile.

#### 3.1.1 Material preparation

Pure copper was selected as the testing material for its good plasticity and the simplicity of microstructure. Three scaled samples with the same height/diameter ratio of 1.5:1 were prepared using super precision wire cutting. The diameter of the samples is 0.5, 1.0 and 2.0 mm, respectively. To obtain different grain sizes, heat treatment of the samples was conducted under different temperatures and holding times in an argon gas filled chamber. Table. 1 shows the heat treatment specifications. After annealing, the metallographic examination was done with the

specimens etched in a solution of 5 g of $FeCl_3$, 15 ml of HCl and 85 ml of $H_2O$ for 15 s. Fig. 2 presents the microstructures and the average grain sizes of the samples. The grain size was measured according to ASTM, using the mean intercept distance method. More than three sections were chosen for one sample to measure the grain size. The average grain size and the deviation are listed in Table. 1. It was found that recrystallization took place in all the specimens, and equiaxed grains were formed.

**Table. 1.** Heat treatment process and the obtained grain sizes

| Diameter (mm) | Temperature (°C) | Dwelling time (h) | Average grain size (μm) | Grain size deviation (μm) |
|---|---|---|---|---|
| 2 | 700 | 2 | 17.4 | 2.1 |
| | 800 | 1 | 53.1 | 5.3 |
| | 850 | 3 | 111.4 | 24.1 |
| 1 | 700 | 2 | 23.5 | 3.5 |
| | 800 | 1 | 49.1 | 3.4 |
| | 850 | 3 | 96.7 | 20.7 |
| 0.5 | 550 | 1 | 16.9 | 6.6 |
| | 650 | 3 | 40.1 | 10.6 |
| | 850 | 3 | 123.4 | 23.2 |

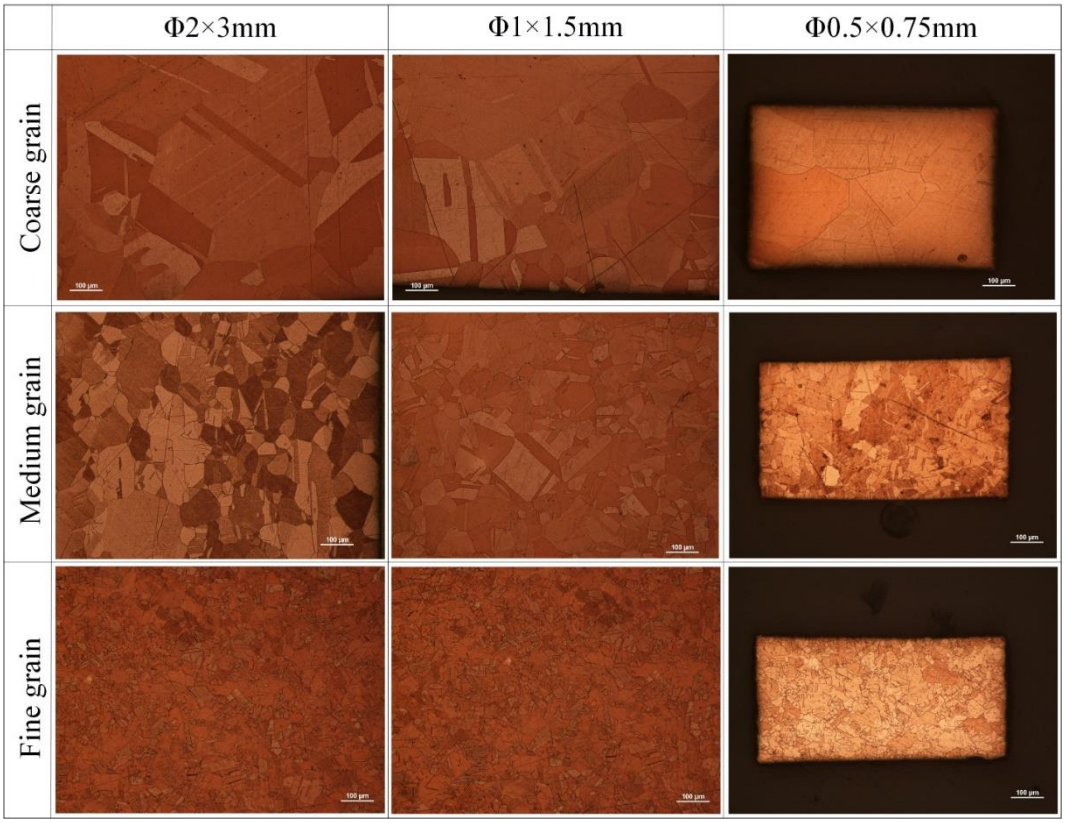


**Fig. 2.** Microstructures of the copper cylindrical samples heat treated by different processes

3.1.2 Barreling compression tests

The compression tests were conducted in a MTS testing machine with the load cell capability from 1 to 50 KN to measure the forming load of the sample. The displacement of punch was recorded and well controlled with an extensometer. Fig. 3 shows the testing platform. Before the test, all the dimensions and heights of the samples were measured with a micrometer. Three compression reductions of 25, 50 and 75% were selected for the compression.

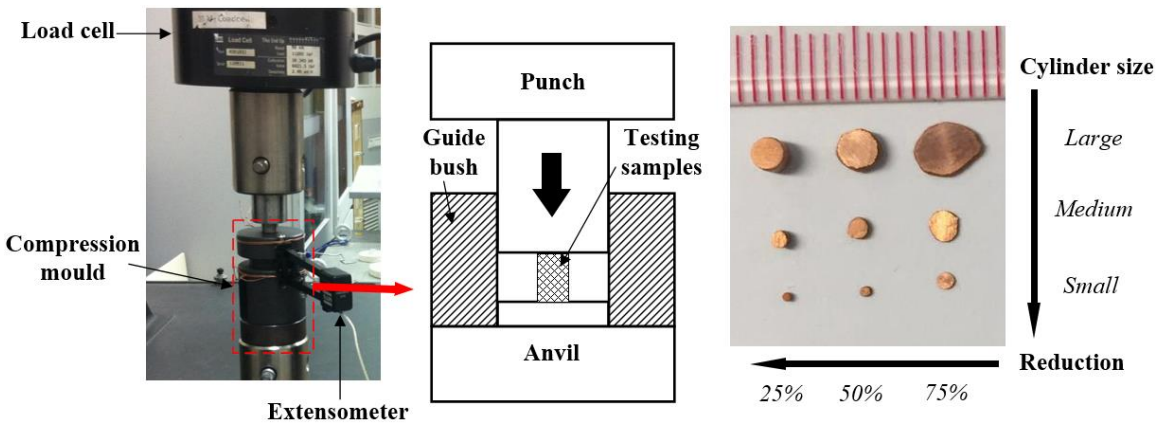


**Fig. 3.** Test platform of workpieces compression

3.1.3 Measurement of the barreling shape of the compressed workpiece

The most widely used method is to measure the radius of different sections of the sample in height direction and plot the obtained radius according to the location of the section to find the shape of geometry. Such a kind of method is applicable in macro-scaled deformation test, since the geometry shape in that scenario is approximately the barreling shape and the shape of the contact surface is almost a circle. So the radius can be measured directly. However, in micro-scaled deformation test, the deformation of the sample is quite irregular due to the crystal anisotropy [18], which makes the geometry shape quite different from the barreling shape. Thus the direct measurement of radius is not reasonable.

In order to deal with the problem, the distribution of the section area $A_i$ was employed to represent the barreling shape in this study. An equivalent radius $R_i$ was calculated based on the section areas, as shown in Fig. 4. Eq.(1) is the expression of $R_i$.

$$R_i = \sqrt{\frac{A_i}{\pi}} \tag{1}$$

where $A_i$ is the area of section i.

According to the volume constancy, the distribution of the section areas in the direction of height reflects the distribution of the average compression strain. It is more related to the definition of barreling than the geometry shape. In addition, the section area contains the message of both the interfacial friction and crystal anisotropy, since the peak and valley contribute to the section area, which further affect the calculated barreling parameter. The equivalent radius calculated in this study is thus reliable in the study of barreling.

To measure the section area, all the compressed samples were scanned with a laser scanning microscope, and the 3D models of the samples were established via combining the front and back halves together, as shown in Fig. 4. To ensure the accuracy of the measurement, the side face was well chosen.

With the 3D models of the samples, the compressed samples were divided into 10 parts averagely according to the height. The total 11 data points (9 intersections, top and bottom surfaces) were obtained in one sample. The section area of the cutting sections was measured using the post-processing software.

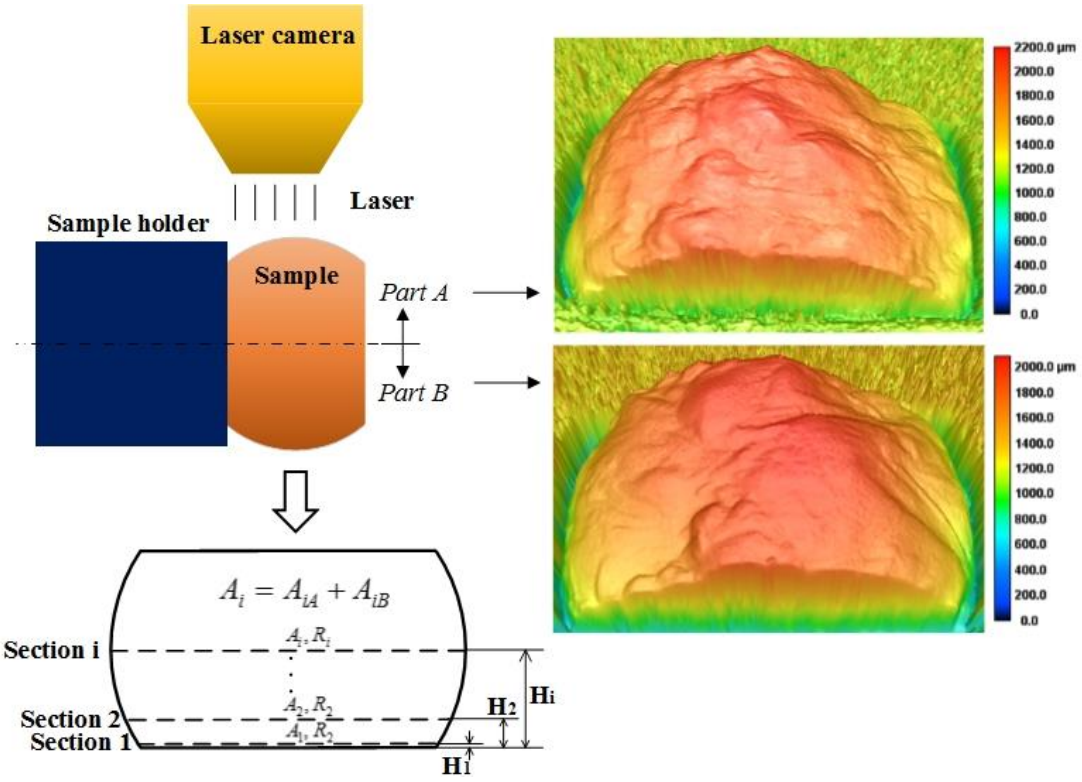


**Fig. 4.** Measurement of section areas

## 3.2 Phenomenon of size effect

### 3.2.1 Shape of side wall

Fig. 5 presents the SEM images of specimens upon the compression of 50%. The valleys and peaks were found on the side surface of the strained workpieces with different grains and dimensions. It is believed to be caused by the inhomogeneous orientation distribution of grains inside the specimens and the anisotropy of grains [17, 44]. The significance of the inhomogeneous deformation decreases with the increase of workpiece size as well as the decrease of grain size of material.

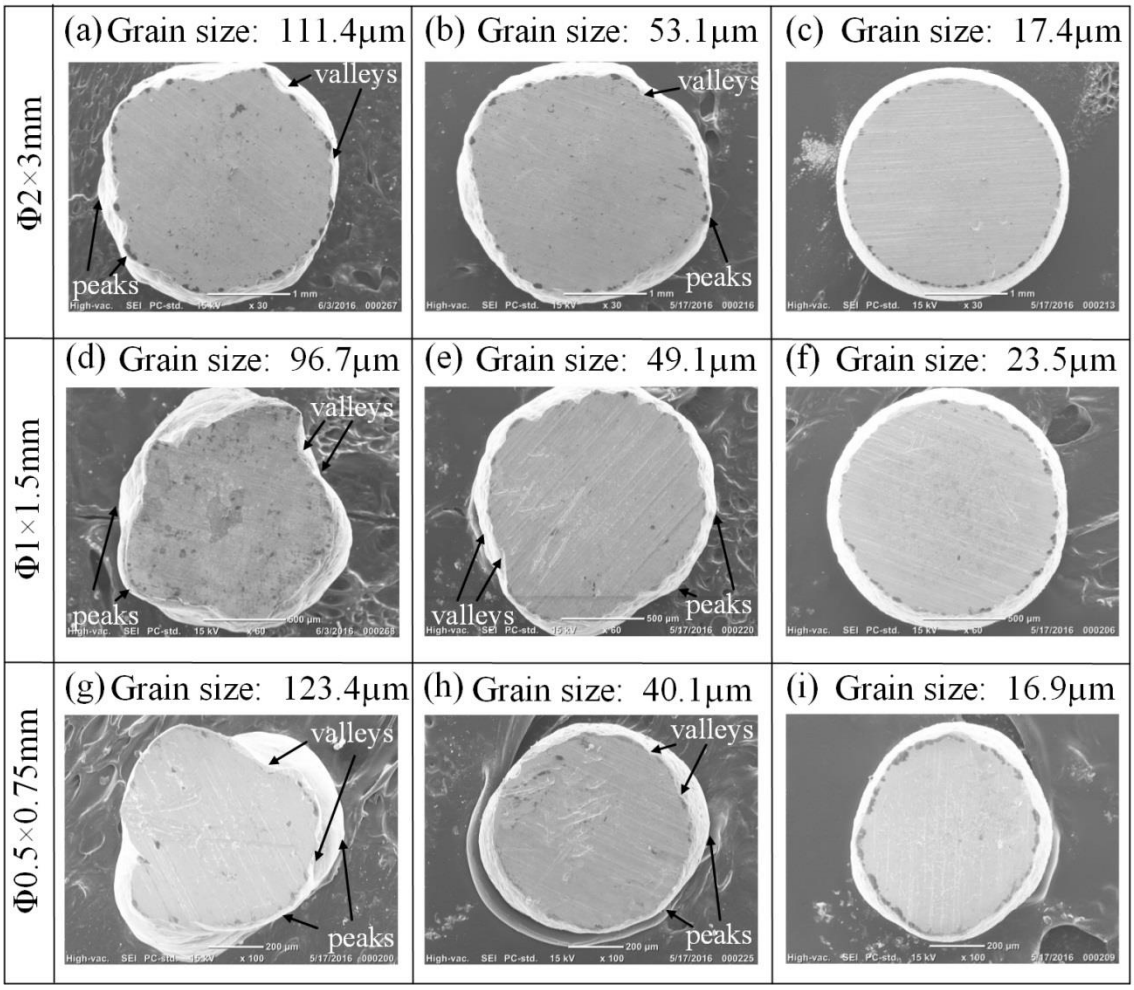


**Fig. 5.** SEM images of the specimens compressed of 50% with different grains and dimensions

Fig. 6 shows the ratio of equivalent radius after compression to initial radius of the specimen, $R_i/R$, of the different sized workpieces with different grains upon compression reduction of 25, 50 and 75%. It is obvious that the equivalent radius is about 2 times the initial radius at the compression reduction of 75%, 1.4 times at 50% and 1.1 times at 25%. The equivalent radius of the section near the end surface is mostly smaller than that at the middle of the workpiece. More importantly, both the value and the comparison of the radius of middle section and the side section is similar to the observations in macro scaled compression scenario [49]. For the cases of

the small size and coarse grains, there are only 3~5 grains across the diameter of the workpieces, and even a concave is observed at the middle of geometry, the equivalent radius of the middle section is still larger than the side one. Since the profile on one side is depressed, it must bulge more on the other side. It means the interfacial friction still causes heterogeneous deformation (barreling) in micro- and meso-scaled samples, regardless of the irregularity of geometry shape caused by the crystalline anisotropy.

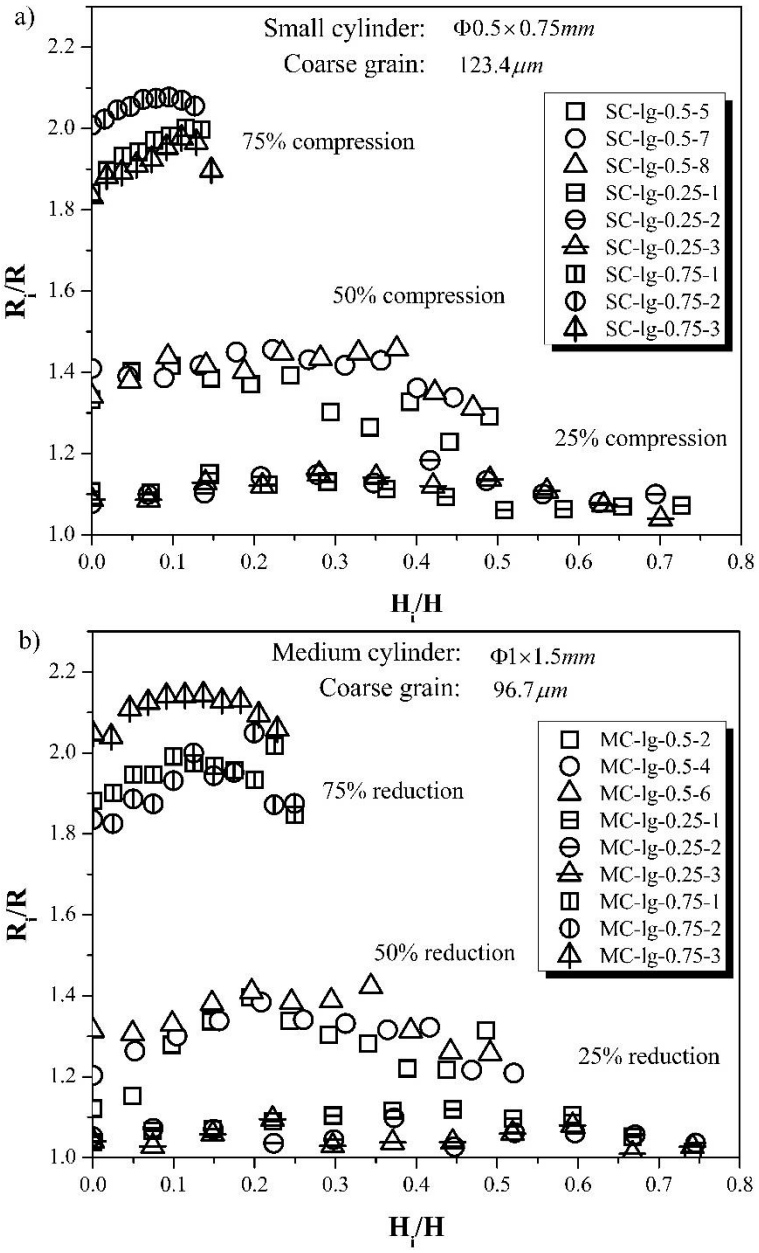

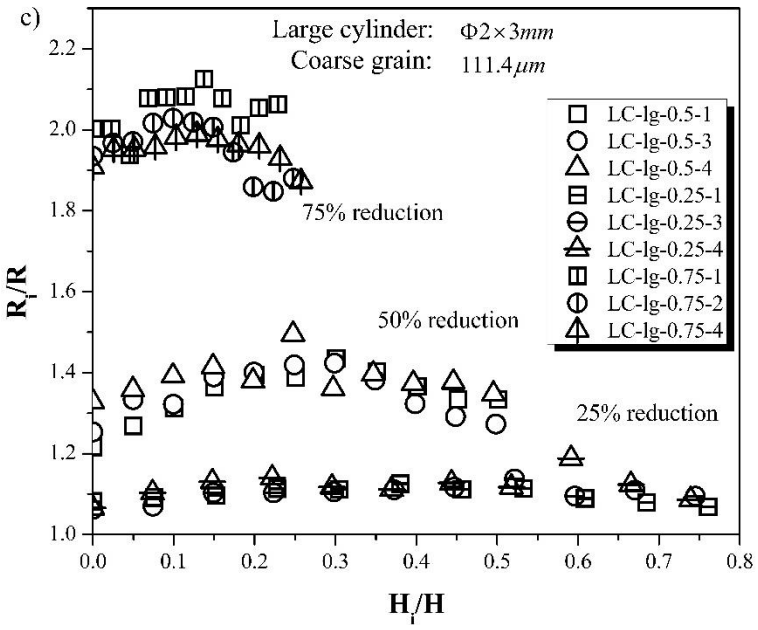
c)
Large cylinder: Φ2×3mm
Coarse grain: 111.4μm
LC-lg-0.5-1
LC-lg-0.5-3
LC-lg-0.5-4
LC-lg-0.25-1
LC-lg-0.25-3
LC-lg-0.25-4
LC-lg-0.75-1
LC-lg-0.75-2
LC-lg-0.75-4
75% reduction
50% reduction
25% reduction
R_i/R
H_i/H

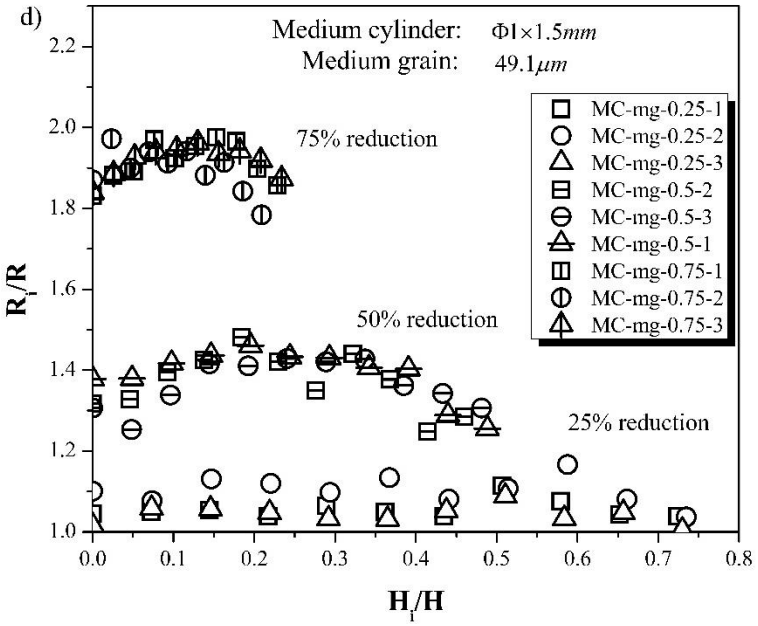
d)
Medium cylinder: Φ1×1.5mm
Medium grain: 49.1μm
MC-mg-0.25-1
MC-mg-0.25-2
MC-mg-0.25-3
MC-mg-0.5-2
MC-mg-0.5-3
MC-mg-0.5-1
MC-mg-0.75-1
MC-mg-0.75-2
MC-mg-0.75-3
75% reduction
50% reduction
25% reduction
R_i/R
H_i/H

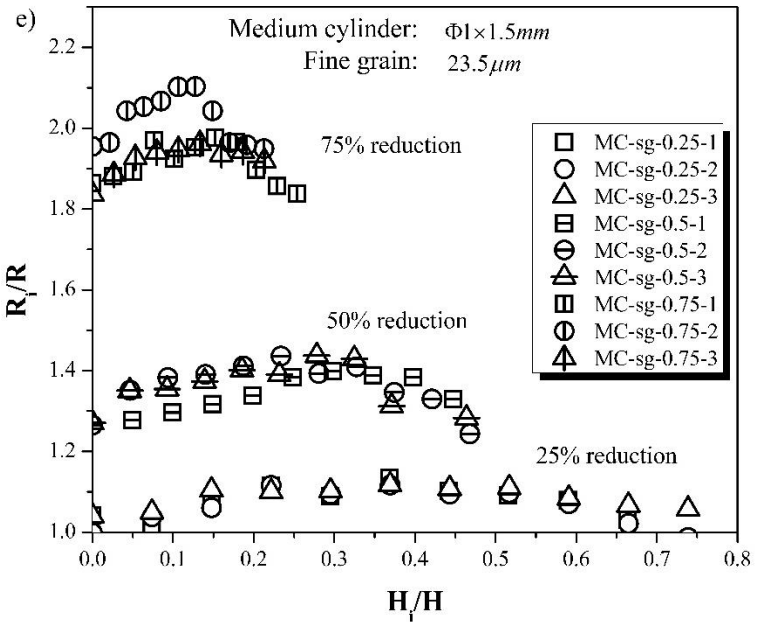


**Fig. 6.** The barrel shape of workpieces: a) Large workpiece with coarse grains, b) Medium workpiece with coarse grains, c) Small workpiece with coarse grains, d) Medium workpiece with medium grains, and e) Medium workpiece with fine grains

3.2.2 Size effect on heterogeneous deformation caused by surface friction.

To make the results comparable for different samples, a non-dimensional barreling shape parameter, $\varphi$, was employed to have an in-depth study of size effect on heterogeneous deformation caused by surface friction. It is designated as follows [41]

$$\varphi = \frac{D_{\mathrm{m}} - (D_{cu} + D_{cb})/2}{H_r} \tag{2}$$

where $D_m$, $D_{cu}$ and $D_{cb}$ represent the diameters of middle plane, upper and bottom contact surfaces, respectively. $H_r$ is the obtained height after compression. For the macro scaled samples, the middle plane is always the largest bulging plane. While for micro scaled samples, due to the inhomogeneous deformation, the equivalent radius obtained in Eq. (1) is used, and as the largest bulging plane is probably not in the middle, the maximum section diameter is thus used instead

of the diameter of middle plane to make the parameter more available for both the meso- and micro- scaled samples. The expression of barreling parameter in this study is given as follows:

$$\varphi = \frac{2R_{\mathrm{m}} - (R_{cu} + R_{cb})}{H_r} = \frac{2\sqrt{\frac{A_m}{\pi}} - (\sqrt{\frac{A_{cu}}{\pi}} + \sqrt{\frac{A_{cb}}{\pi}})}{H_r} \quad (3)$$

Fig. 7 shows the grain size effect on the barreling of different sized samples with all the compression reductions. A similar phenomenon that the barreling parameter increases with the decrease of grain size is easy to be observed in the large and medium sized samples. In Fig. 7 a) and b), a monotonically increasing tendency of the barreling parameter is obvious for both the sized samples upon the compression of 25%.

However, the relation between grain size and barreling degree becomes uncertain when the compression is increased to 50 and 75% for the large and medium workpieces, as shown in Fig. 7 a) and b). Although the monotonically increasing tendency was also observed for the large workpieces with the compression ratio of 75% and the medium workpieces under the compression of 50%, the large error bar makes the dependency of barreling on grain size to be weaker. The samples with coarse grains deformed at the compression of 50% for the large workpieces and 75% for the medium workpieces reveal the opposite results to those deformed at the compression of 25%.

For the small workpiece, the grain size effect is quite different. As shown in Fig. 7 c), when the workpieces undergo the compression of 25%, the barreling shape parameter, φ decreases first, and then increases, with the grain size decreases from 123.4 to 16.9 μm. When the compression reduction is increased to 50% and 75%, however, the barreling shape parameter of the coarse grained samples seems smaller than that with medium grains. Actually, it is due to the cracks in

the samples with the large grain size. Fig. 8 shows the SEM image of the cracks on the surface of a small workpiece with large grains and the compression reduction is 50%. The cracks released the stress on the surface, and extended the diameter of the surface. Thus the barreling shape parameter decreases.

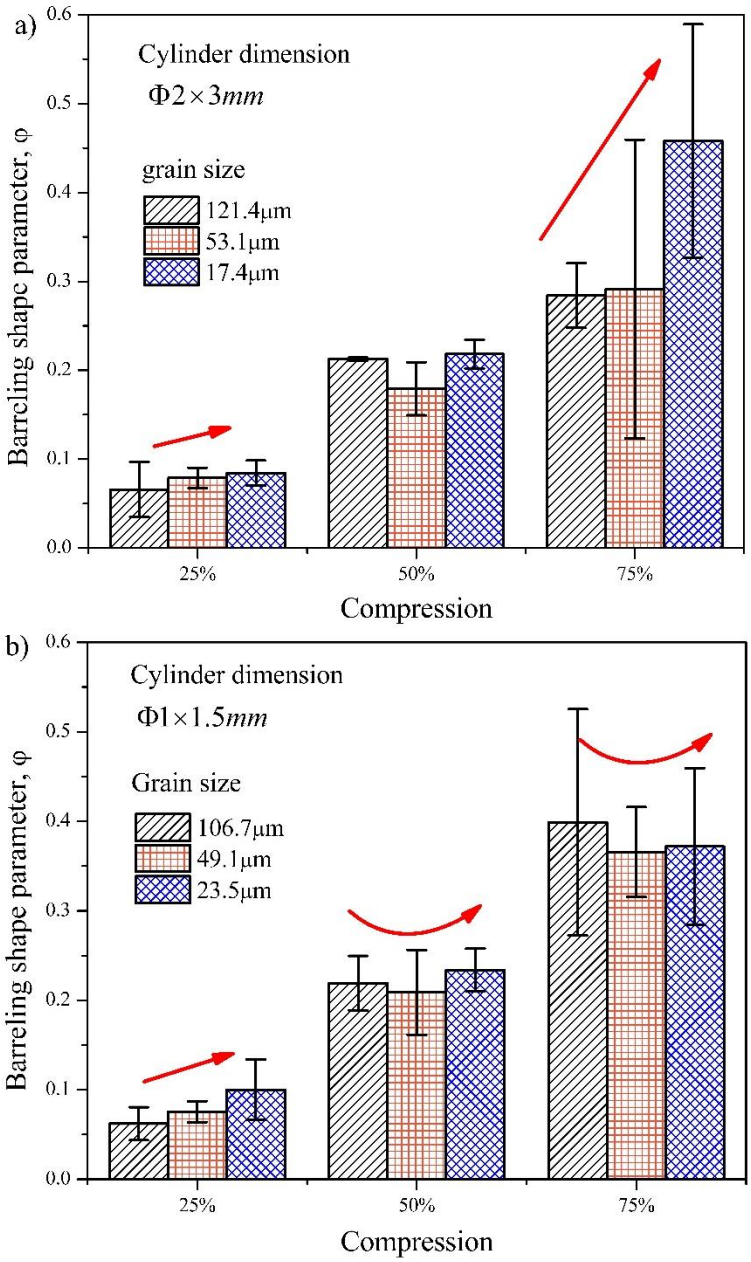
a)
Cylinder dimension
Φ2×3mm
grain size
121.4μm
53.1μm
17.4μm
Barrcling shapc paramcter, φ
0.0
0.1
0.2
0.3
0.4
0.5
0.6
25%
50%
75%
Compression
b)
Cylinder dimension
Φ1×1.5mm
Grain size
106.7μm
49.1μm
23.5μm
Barreling shape parameter, φ
0.0
0.1
0.2
0.3
0.4
0.5
0.6
25%
50%
75%
Compression

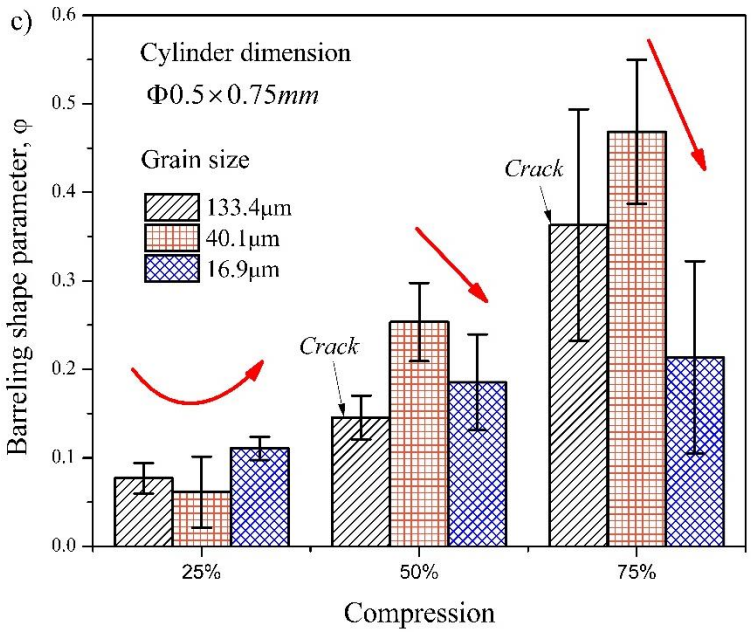


**Fig. 7.** Effect of grain size on relative barrel dimension under different compressions a) large workpieces, b) medium workpieces, c) small workpieces

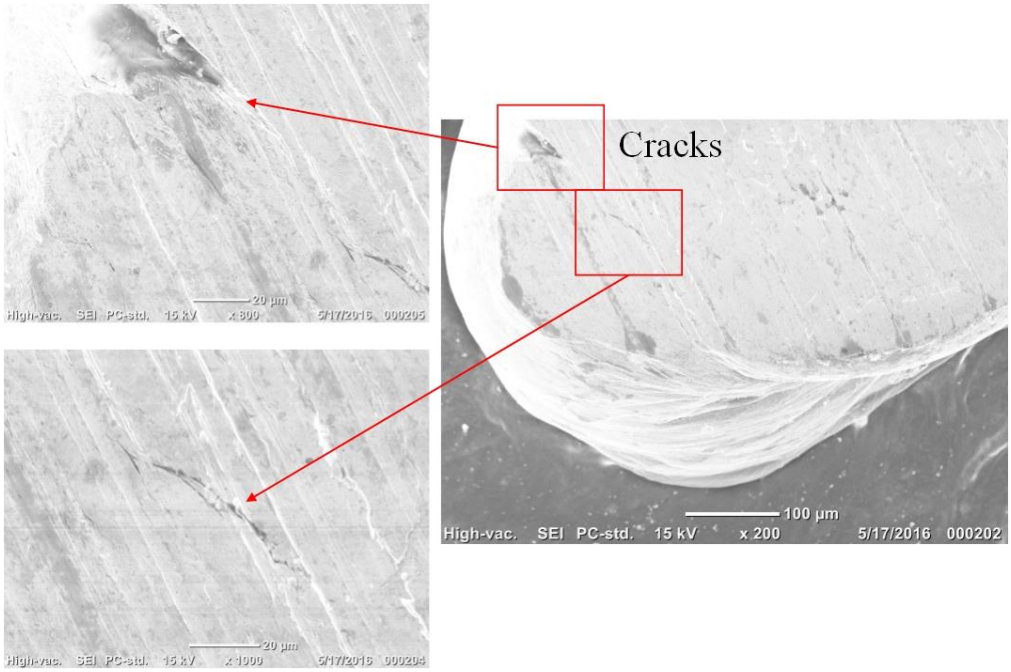


**Fig. 8.** SEM image of the cracks on the surface of small workpieces with large grains

To have a direct view of size effect on barreling phenomenon, the evolution of barreling shape parameter from micro- to meso-scale is represented by a function of scale factor d/R, as illustrated in Fig. 9. It is found that when the compression is 25%, the average value of barreling shape parameter decreases first and then increases with the reciprocal of scale factor, R/d, increases from 2 to 60, while the scatter of the measured value increases first then decreases. And the case with the lowest average value reveals the largest scatter. Obviously, the dependence of barreling degree on the scale factor changes, which means more than one reasons should be responsible for the size effect. And these reasons are probably the microstructure size and surface constraints. Notably, the barreling shape parameter obtained with the compression of 50% and 75% is not compared here because the crack and foldover makes the reasons for barreling shape more complex [31].

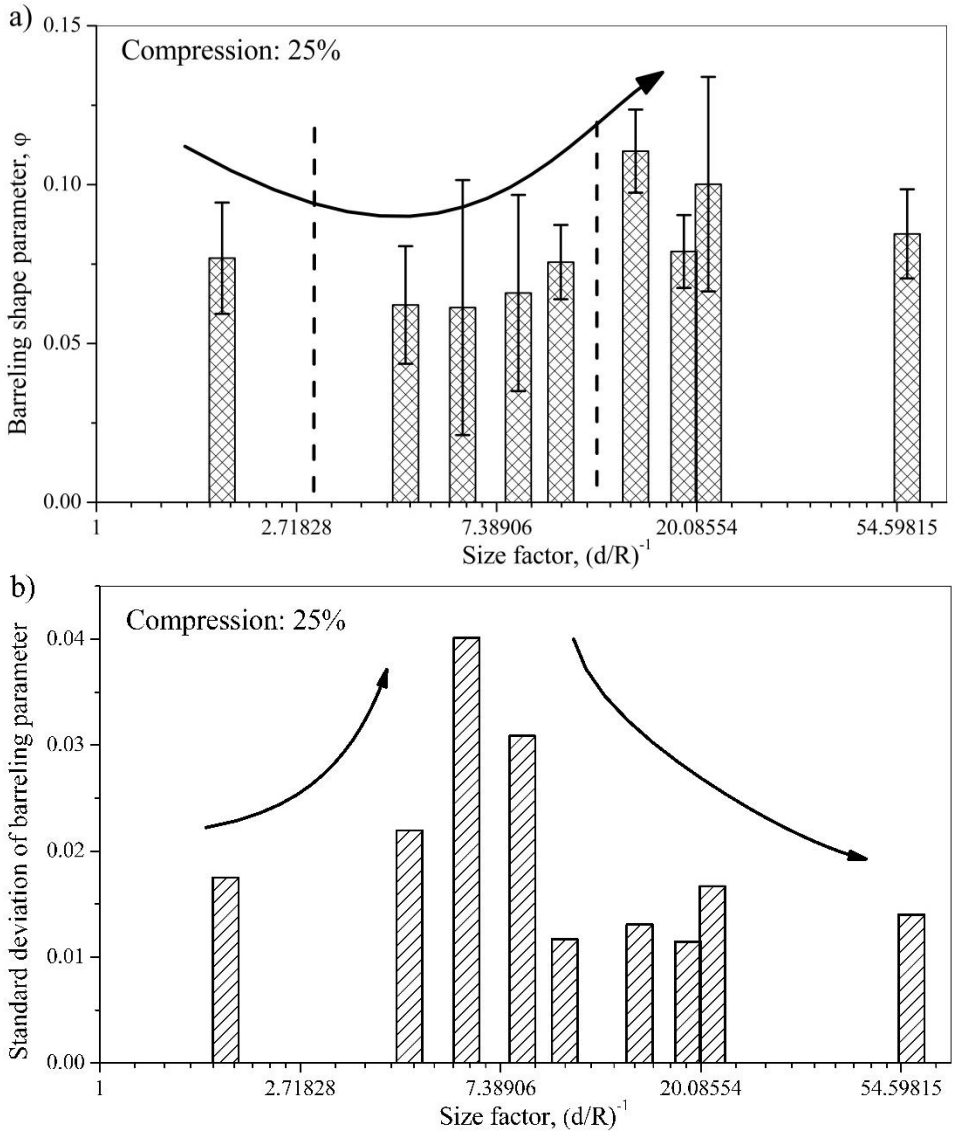


**Fig. 9.** The evolution of barreling from micro scale to macro scale under a) average value, b) scatter value

## 3.3 Microstructures after deformation

The samples as shown in Fig. 9 a) are classified into three categories according to the barreling shape parameter indicated by the dashed lines in the figure. The representative sample of each category is chosen to be further tested using metallography observation, and the microstructures are shown in Fig. 10. For the large workpiece, deformation bands are observed in the inner

grains and distributed along the diagonal lines, as shown by the dashed line in Fig. 10 a). It is similar to the observations in the macro-scaled upsetting deformation [30]. Seldom deformation bands are found in surface grains of large workpieces. For the medium workpiece, as shown in Fig. 10 b), the surface grains take a large part in the section, and thus few deformation bands are observed in the section of workpiece. Grains seem to be rotated to form the bulge shape. For the small workpiece, with the further decrease of dimension, the surface grains takes a larger part in the section than medium workpiece, as shown in Fig. 10 c), however, much more deformation bands are observed over the section of workpiece.

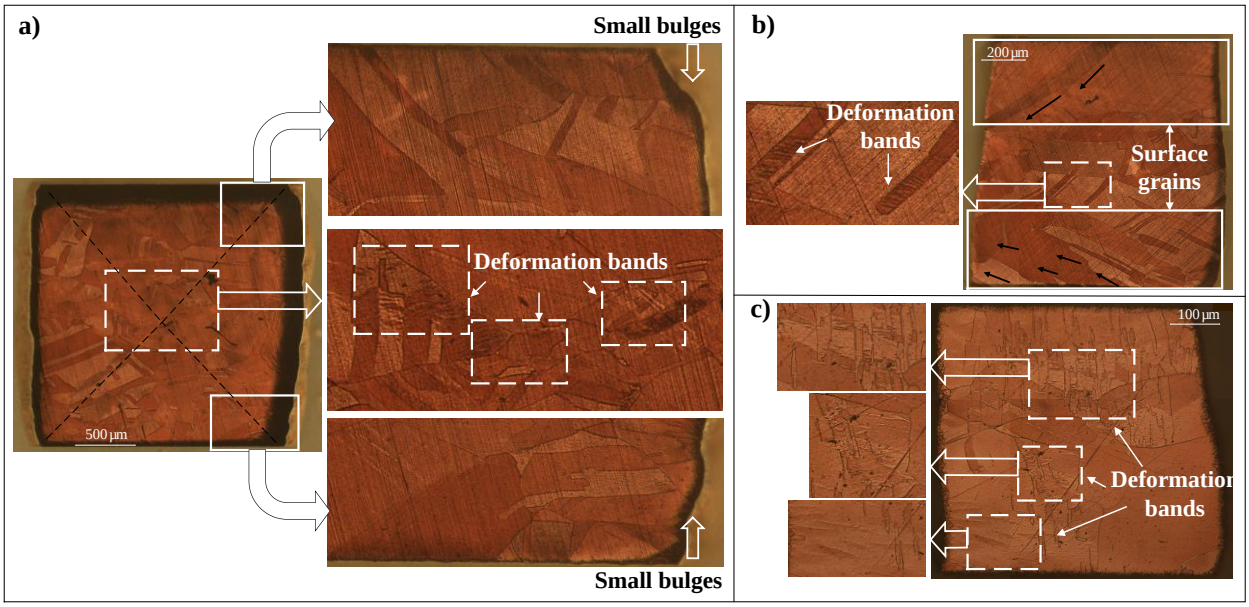


**Fig. 10.** Microstructures of the samples with large grains under the compression of 25% a) large workpiece, b) medium workpiece and c) small workpiece.

As is known, the deformation bands always take place in the deformation of polycrystalline and constrained single crystalline materials. Since in such a kind of materials, grain rotation is always constricted and the deformation is not satisfied with the primary main slip only, but also with extra minority secondary slip. The appearance of secondary slip is the main reason of the

formation of deformation bands [50]. However, for a free grain without any constraint, it tends to rotate firstly to have a preferred orientation compatible with the applied stress, so that few secondary slips are started, and thus few deformation bands are observed.

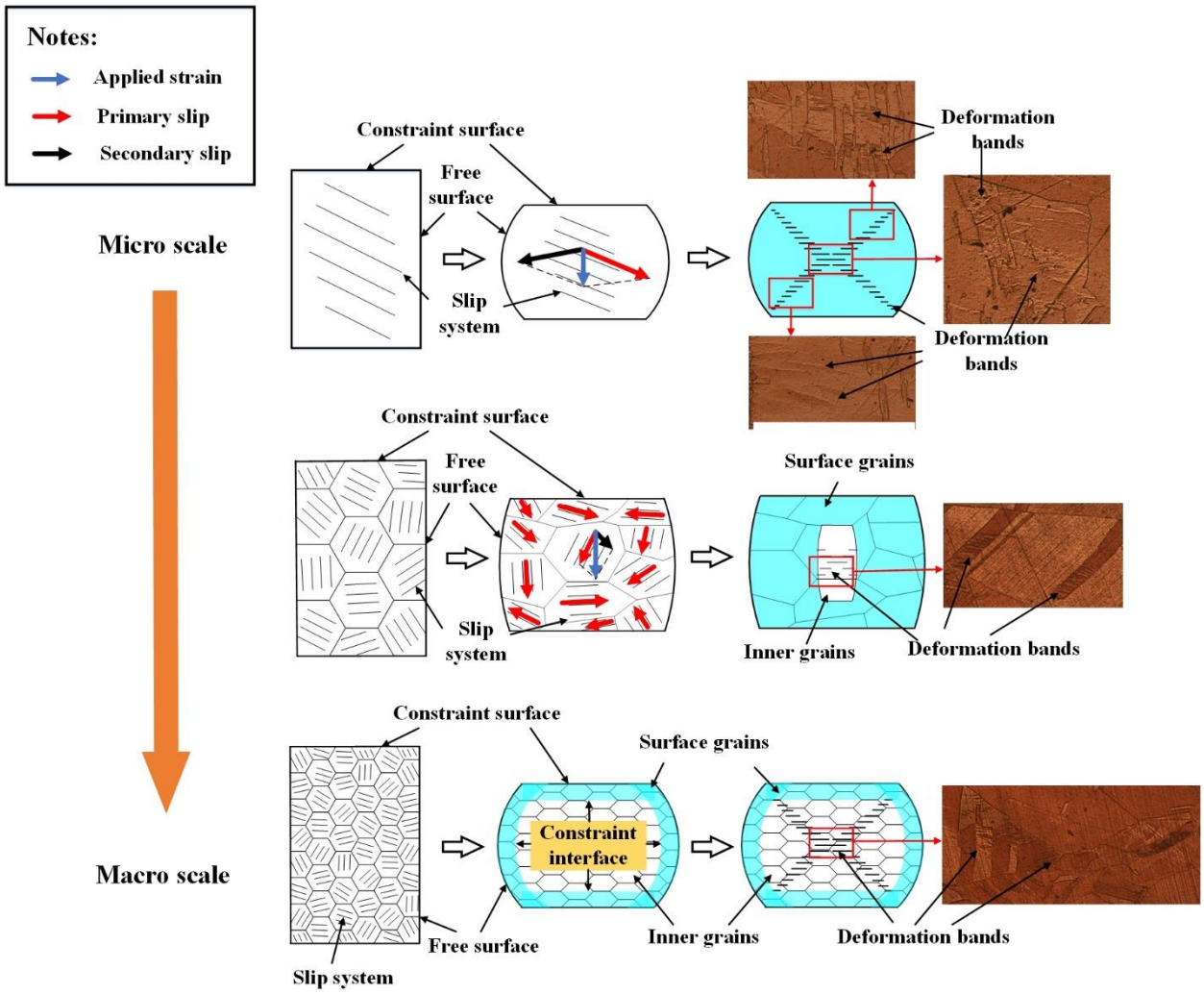


**Fig. 11.** Size effect on plastic deformation under the co-effect of microstructure and surface constraints

Thus the distribution of deformation bands reveals the restrictions to grains. In the uniaxial compression process, the restrictions to grains mainly come from external boundary condition and neighbor grains. As shown in Fig. 11, for micro scaled specimen, as there are only a few

grains exist in the specimen, the grains are mainly restricted by the tooling. To satisfy the displacement of tools, the secondary slip must occur and thus the deformation bands appear. With the increase of grain number in the specimen, there are more strain directions for the main slip of grains. As the side walls of the specimen are free surfaces and the specimen is mostly constructed with surface grains, the overall deformation can be satisfied by the compatibility of the slip of soft oriented grains and the rotation of hard oriented grains. Therefore, the number of deformation bands is decreased with the increase number of grains. With the further increase of grain number, inner grains increase in the specimen. As inner grains are restricted by neighbor grains, in order to satisfy the overall deformation, the secondary slip of hard oriented grains must occur. In this period, the increase of grain number results in an increasing deformation bands.

In Fig. 10, the large workpiece is polycrystalline and the small workpiece is similar to the constrained single crystalline materials. Thus both of them contain deformation bands. However, the medium workpiece is different since it is in the middle of single crystalline and polycrystalline materials, where both of the constraints may be the weakest and the grain rotation is much easier than that in other cases.

## 4 Extended upper bound solution

In order to have a direct view of the interaction of different constrains, an extended upper bound solution of the barreling degree in compression process considering both effects of inter-grain restrictions and external constraints was established.

### 4.1 Modeling

#### 4.1.1 Descriptions of the constraints

(1) Inter-grain restrictions

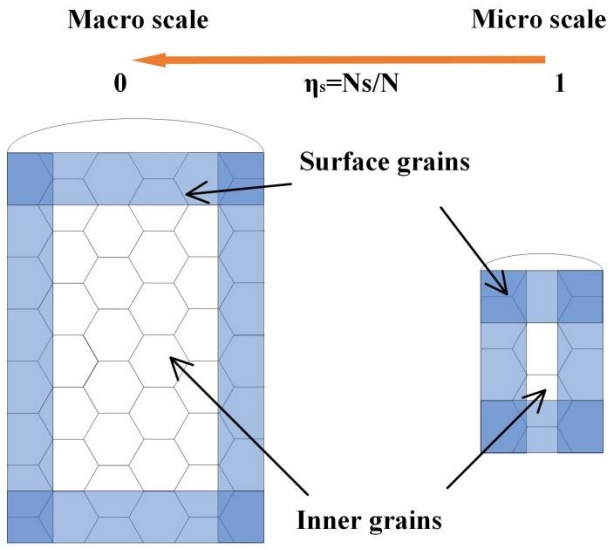


**Fig. 12.** Distribution of the surface grains in the section of cylindrical samples

The inter-grain restriction can be generally described using the surface layer model, as shown in Fig. 12. According to surface layer model [10], the inner grains are covered by a layer of surface grains. With the decrease of workpiece size, the proportion of the surface grains increases. It is claimed that the grains located at the free surface are less restricted than the interior grains. It leads to the lower resistance against the deformation of surface grains, since the dislocations moving through the grains during the deformation process do not pile up at the free surface. So when the share of surface grains increases, the flow stress of surface grains contributes more to the overall flow stress of the sample.

Based on the surface layer model [10], the flow stress of the workpiece can be expressed as:

$$\sigma = \frac{N_s\sigma_s + N_i\sigma_i}{N} = \eta_s\sigma_s + (1-\eta_s)\sigma_i \tag{4}$$

where $\sigma$ is the flow stress of the material; $N_s$ and $N_i$ are the numbers of surface grains and inner grains; $N=N_s+N_i$ is the total number of grains; $\sigma_s$ is the flow stress of the surface grains and $\sigma_i$ is

the flow stress of the inner grains. $\eta_s$ is the ratio of the surface grains to the overall grains, viz., $N_s$ /$N$.

According to Peng et al. [11], the surface grains can be regarded as single crystal, while the inner grains are considered as polycrystal. Based on crystal plastic theory and Hall-petch equation, the flow stresses of surface and inner grains are designated as:

$$\begin{cases} \sigma_s(\varepsilon) = m\tau_R(\varepsilon) \\ \sigma_i(\varepsilon) = M\tau_R(\varepsilon) + \dfrac{k(\varepsilon)}{\sqrt{d}} \end{cases} \tag{5}$$

M and m are the orientation factors of polycrystal and single crystal respectively, which are not related to the grain size or strain [51, 52]. $\tau_R(\varepsilon)$ is the lattice friction stress of single crystal. k($\varepsilon$) is the locally intensified stress needed to propagate general yield stress across the polycrystal grain boundaries [53] and d is the grain size. As both $\tau_R(\varepsilon)$ and k($\varepsilon$) can be represented by exponential function of $y = kx^n$ [54], Eq.(4) is further deduced to

$$\sigma = \eta_s m k_0 \varepsilon^{n_1} + (1-\eta_s)\left( M k_0 \varepsilon^{n_1} + \frac{k_m \varepsilon^{n_2}}{\sqrt{d}} \right) \tag{6}$$

where $k_0$, $k_m$, $n_1$and $n_2$ are the constants independent of dimension or grain sizes.

(2) External constraints

The external constraints are mainly from the tool-workpiece interface. The interfacial friction stress can be described by constant friction factor theory, which is expressed as follows:

$$\tau_s = fK \tag{7}$$

where f is the friction factor and K is the shear stress of the material. If Mises yielding criterion is used, K = $\sigma/\sqrt{3}$. So the friction stress is obtained as:

$$\tau_s = f\sigma/\sqrt{3} \tag{8}$$

4.1.2 Upper bound solution

The upper bound theorem states that among all the kinematically admissible strain rate fields, the actual one minimizes the following function, which is the dissipated energy of the deformation body represented by different dissipated energies consumed in different deformation sources [39]

$$J = \int_V \sigma\sqrt{\frac{2}{3}\dot{\varepsilon}_{ij}\dot{\varepsilon}_{ij}}\,dV + \int_S K|\Delta V_i|dS + \int_{S_m} fK|\Delta V_i|dS - \int_{S_T} T_i V_i dS \tag{9}$$

The first term in Eq. (9) is the internal power of deformation represented by strain rate. The second and third terms express the power consumed due to the shearing deformation over the surface of velocity discontinuities and the power to overcoming the friction at the interfaces between the tool and the material, respectively. The last term reflects the power done by the predetermined body traction.

Fig. 13 shows the compression of a workpiece in a cylindrical coordinate system. The specimen with a height of H and a radius of R is compressed by the upper and the bottom platens, which move toward each other at the same velocity of $\dot{u}$. The radial velocity at the contact layer of the disk is smaller than that at the middle due to friction, resulting in the barreling effect. The equivalent barreling shape obtained in this study (shown in Fig. 6) confirms this velocity assumption. Avitzur [38] used an exponential law to approximate the velocity boundary, and the velocity field in the cylindrical workpiece can be expressed as follows:

$$\begin{aligned} \dot{u}_r &= \frac{1}{4}\frac{b}{1-e^{-b/2}}\dot{u}\frac{r}{H}e^{-by/H} \\ \dot{u}_y &= -\frac{\dot{u}}{2}\frac{1-e^{-by/H}}{1-e^{-b/2}} \\ \dot{u}_\theta &= 0 \end{aligned} \tag{10}$$

In the above velocity field, R and H are the geometry parameters representing the diameter and height of workpiece respectively. b is the barreling parameter for describing the degree of barreling.

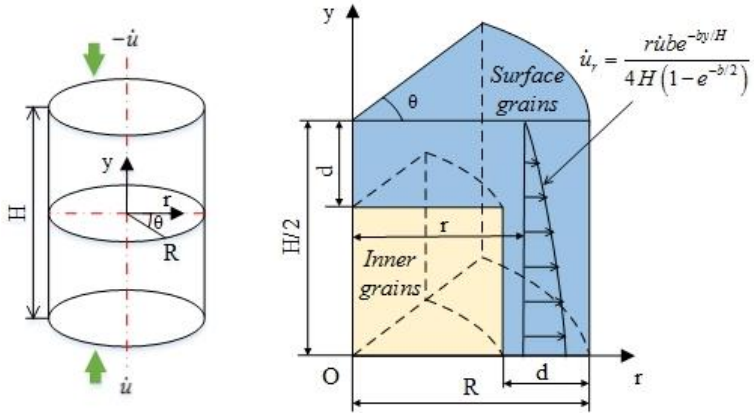


**Fig. 13.** A Schematic diagram of the cylindrical coordinate system in the workpiece compression

Based on the assumed velocity field, the strain rate is obtained in the following:

$$\begin{aligned}
\dot{\varepsilon}_{rr} &= \frac{1}{4}\frac{b}{1-e^{-b/2}}\frac{\dot{u}}{H}e^{-by/H} \\
\dot{\varepsilon}_{\theta\theta} &= \frac{1}{4}\frac{b}{1-e^{-b/2}}\frac{\dot{u}}{H}e^{-by/H} \\
\dot{\varepsilon}_{yy} &= -\frac{1}{2}\frac{b}{1-e^{-b/2}}\frac{\dot{u}}{H}e^{-by/H} \\
\dot{\varepsilon}_{ry} &= -\frac{1}{8}\frac{b^2}{1-e^{-b/2}}\frac{\dot{u}r}{H^2}e^{-by/H} \\
\dot{\varepsilon}_{r\theta} &= \dot{\varepsilon}_{y\theta} = 0
\end{aligned} \tag{11}$$

The equivalent strain rate is thus determined as:

$$\dot{\varepsilon}_I^e = \sqrt{\frac{2}{3}\dot{\varepsilon}_{ij}\dot{\varepsilon}_{ij}} = \frac{1}{2}\frac{b}{1-e^{-b/2}}\frac{\dot{u}}{H}e^{-by/H}\sqrt{1+\frac{b^2r^2}{12H^2}} \tag{12}$$

In compression process, as there is no velocity discontinuities or body tractions, internal deformation and friction loss at the specimen-workpiece interfaces are the main energy dissipation. Thus Eq.(9) is simplified as follow:

$$J = \int_{V_I} \sigma \dot{\varepsilon}_I^e dV + \int_{S_m} fK \left|\Delta V_i\right|_s dS \tag{13}$$

where $V_I$ represents the volume of the workpiece. $S_m$ is the face of the tool-workpiece contacting surface. The sliding velocities on the tool-workpiece interface are obtained from Eq.(11).

On the contacting surface, the sliding velocity is expressed as:

$$\left|\Delta V_i\right|_m = \frac{rb\dot{u}}{4H} \frac{e^{-b/2}}{1-e^{-b/2}} \tag{14}$$

Hence, for the compression of macro scaled workpiece, the total energy required can be calculated by substituting Eqs. (12) and (14) into Eq.(13).

If the dimension of the specimen is scaled down to micro scale, where the proportion of surface grains, $\eta_s$, is unneglectable, the power equation should be further extended due to the difference between the flow stress of surface grains and inner grains. If the width of the surface region is uniform in both the head and side faces of the workpiece, $\eta_s$ can be formulated as:

$$\eta_s = 1 - \frac{(R-d)^2 (H-2d)}{R^2 H} = 1 - (1-\eta)^2 \left(1 - \frac{2R}{H}\eta\right) \tag{15}$$

where $\eta = \frac{d}{R}$ is the scale factor in this study.

As shown in Fig. 13, the workpiece contains both the surface and inner regions, thus the internal deformation energy covers the surface and inner parts. Eq.(13) is thus further extended into Eq.(16) in the following:

$$J = \int_{V_I^s} \sigma^s \dot{\varepsilon}_I^e dV + \int_{V_I^i} \sigma^i \dot{\varepsilon}_I^e dV + \int_{S_m} fK\left|\Delta V_i\right|_s dS \tag{16}$$

where $\sigma^s$, $\sigma^i$, $K^s$, $K^i$ are the flow and shear stresses of the surface and inner grains, respectively.

For a given geometry of H >R, the terms in the right hand of Eq.(16) are formulated as:

$$\begin{aligned}
&\int_{V_I^s} \sigma^s \dot{\varepsilon}_I^e dV = 4\pi \int_{H/2-w}^{H/2} \left( \int_0^{R-w} r\sigma^s \dot{\varepsilon}_I^e dr \right) dy + \int_0^{H/2} \left( \int_{R-w}^{R} r\sigma^s \dot{\varepsilon}_I^e dr \right) dy \\
&\int_{V_I^i} \sigma^i \dot{\varepsilon}_I^e dV = 4\pi \int_0^{H/2-w} \left( \int_0^{R-w} r\sigma^i \dot{\varepsilon}_I^e dr \right) dy \\
&\int_{S_m} fK^s \left|\Delta V_i\right|_s dS = 4\pi f \int_0^R rK\left|\Delta V_i\right|_s dr
\end{aligned} \tag{17}$$

By substituting Eqs. (12), (15) and (17) into Eq.(16), the total required energy for compression is denoted as a function of material parameters (M and m), scale factor (η), friction factor (f), and the barreling parameter (b). The detailed expressions are listed as follows.

The strain dissipation energy of the surface grains is

$$\begin{aligned}
\dot{w}_{Is} &= 4\pi \left( \int_{H/2-w}^{H/2} \left( \int_0^{R-w} r\sigma^s \dot{\varepsilon}_I^e dr \right) dy + \int_0^{H/2} \left( \int_{R-w}^{R} r\sigma^s \dot{\varepsilon}_I^e dr \right) dy \right) \\
&= -\frac{\pi\sigma^s b\dot{u}}{3\sqrt{3}H} \left( \left( \frac{12H^2}{b^2} + \left(R-w\right)^2 \right)^{3/2} \frac{1-e^{(w/H-1/2)b}}{1-e^{-b/2}} - \left( \frac{12H^2}{b^2} \right)^{3/2} \frac{e^{-b/2}-e^{(w/H-1/2)b}}{1-e^{-b/2}} - \left( \frac{12H^2}{b^2} + R^2 \right)^{3/2} \right)
\end{aligned} \tag{18}$$

The strain dissipation energy of the inner grains is:

$$\begin{aligned}
\dot{w}_{Ii} &= 4\pi \int_0^{H/2-w} \left( \int_0^{R-w} r\sigma^i \dot{\varepsilon}_I^e dr \right) dy \\
&= \frac{\pi\sigma^i b\dot{u}}{3\sqrt{3}H} \left( \left( \frac{12H^2}{b^2} + \left(R-w\right)^2 \right)^{3/2} - \left( \frac{12H^2}{b^2} \right)^{3/2} \right) \frac{1-e^{(w/H-1/2)b}}{1-e^{-b/2}}
\end{aligned} \tag{19}$$

The frictional dissipation is

$$\dot{w}_f = 4\pi f \int_0^R rK\left|\Delta V_i\right|_s dr = 4\pi \frac{f\sigma}{\sqrt{3}} \int_0^R r \frac{rb\dot{u}}{4H} \frac{e^{-b/2}}{1-e^{-b/2}} dr = \frac{\pi f \sigma b\dot{u} R^3}{3\sqrt{3}H} \frac{e^{-b/2}}{1-e^{-b/2}} \tag{20}$$

The total dissipation energy is obtained:

$$J = \dot{w}_{Is} + \dot{w}_{Ii} + \dot{w}_f$$

$$= \frac{\pi\sigma^s b\dot{u}}{3\sqrt{3}H}\left(\begin{array}{l}\left(\frac{12H^2}{b^2}+R^2\right)^{3/2}-\left(\frac{12H^2}{b^2}\right)^{3/2}+\frac{\left(\eta+\frac{\sigma^i}{\sigma^s}(1-\eta)\right)fR^3e^{-b/2}}{1-e^{-b/2}} \\ +\left(\frac{\sigma^i}{\sigma^s}-1\right)\left(\left(\frac{12H^2}{b^2}+(R-w)^2\right)^{3/2}-\left(\frac{12H^2}{b^2}\right)^{3/2}\right)\frac{1-e^{(w/H-1/2)b}}{1-e^{-b/2}}\end{array}\right) \tag{21}$$

According to the conservation of energy, the external work is equal to the dissipated energy. Thus the following equation is obtained:

$$J(M,m,f,\eta,b) = \pi R^2 \dot{u} p_{ave} \tag{22}$$

The normalized average forging pressure is obtained by substituting Eq. (21) into Eq. (22) and is further formulated as:

$$\frac{p_{ave}}{\sigma} = \frac{R}{3\sqrt{3}b^2H\left(1+\left(\frac{\sigma^i}{\sigma^s}-1\right)(1-\eta)^2\left(1-\frac{2R}{H}\eta\right)\right)}\left(\begin{array}{l}\left(\frac{12H^2}{R^2}+b^2\right)^{3/2}-\left(\frac{12H^2}{R^2}\right)^{3/2}+\frac{\left(1+\left(\frac{\sigma^i}{\sigma^s}-1\right)(1-\eta)^2\left(1-\frac{2R}{H}\eta\right)\right)b^3fe^{-b/2}}{1-e^{-b/2}} \\ +\left(\frac{\sigma^i}{\sigma^s}-1\right)\left(\left(\frac{12H^2}{R^2}+b^2(1-\eta)^2\right)^{3/2}-\left(\frac{12H^2}{R^2}\right)^{3/2}\right)\frac{1-e^{(\eta R/H-1/2)b}}{1-e^{-b/2}}\end{array}\right) \tag{23}$$

In Eq. (23), the specimen dimension , material parameters, scale factor and the friction factor are intrinsic parameters for compression deformation. Therefore, the principle of minimum energy is employed to determine the velocity field parameter, b. The following equation is thus satisfied:

$$\frac{\partial\left(\frac{p_{ave}}{\sigma}\right)}{\partial b} = 0 \tag{24}$$

According to Eq. (24) the optimized parameter is determined as follows (the details are in Appendix I).

$$b_{opt}=\frac{f-3\sqrt{3}D_1}{\frac{\sqrt{3}}{8}\frac{R}{H}\left(D_3+\sqrt{D_3-\frac{16\sqrt{3}}{3}D_2\left(f-3\sqrt{3}D_1\right)}\right)} \tag{25}$$

where $D_1$, $D_2$ and $D_3$ are size-dependent parameters and given by

$$\begin{aligned}
D_1&=\frac{\eta\left(\frac{\sigma^i}{\sigma^s}-1\right)(1-\eta)^2\left(1-\frac{\eta R}{H/2}\right)}{1+\left(\frac{\sigma^i}{\sigma^s}-1\right)(1-\eta)^2\left(1-\frac{\eta R}{H/2}\right)}\\
D_2&=\frac{\eta\left(\frac{\sigma^i}{\sigma^s}-1\right)(1-\eta)^4\left(1-\frac{\eta R}{H/2}\right)}{1+\left(\frac{\sigma^i}{\sigma^s}-1\right)(1-\eta)^2\left(1-\frac{\eta R}{H/2}\right)}\\
D_3&=\frac{1+\left(\frac{\sigma^i}{\sigma^s}-1\right)(1-\eta)^4\left(1-\frac{\eta R}{H/2}\right)}{1+\left(\frac{\sigma^i}{\sigma^s}-1\right)(1-\eta)^2\left(1-\frac{\eta R}{H/2}\right)}
\end{aligned} \tag{26}$$

## 4.2 Validation

### 4.2.1 Parameters determination

According to Eqs. (25) and (26), the barreling parameter is determined by friction factor f, the flow stress ratio of the surface and inner grains $\frac{\sigma^i}{\sigma^s}$, and the scale parameter η, respectively. Based on Eq.(5), $\frac{\sigma^i}{\sigma^s}$ can be expressed as:

$$\frac{\sigma^i}{\sigma^s}=\frac{M}{m}\frac{k_0{\varepsilon_{inner}}^{n_1}}{k_0{\varepsilon_{surface}}^{n_1}}+\frac{k_m{\varepsilon_{inner}}^{n_2}}{m\sqrt{d}k_0{\varepsilon_{surface}}^{n_1}}=\frac{M}{m}\left(1+\frac{k_m{\varepsilon_{inner}}^{n_2-n_1}}{M\sqrt{d}k_0}\right)\left(\frac{\varepsilon_{inner}}{\varepsilon_{surface}}\right)^{n_1} \tag{27}$$

where $\varepsilon_{inner}$ and $\varepsilon_{surface}$ refer to the strains in the inner and surface grains, respectively. It is found that the ratio increases with the increase of inner strain and the decrease of grain size. However, there is an interaction between these two factors. Since the decrease of grain size

makes the inner grains stronger and the inner grains will have a smaller strain. Thus $\varepsilon_{inner}$ decreases and $\varepsilon_{surface}$ increases, which will reduce the value of $\frac{\sigma^i}{\sigma^s}$.

An approximate relation between $\frac{\sigma^i}{\sigma^s}$ and compression ratio for the small deformation cases is derived based on the equilibrium of force in y direction in this study, as follow (details are in Appendix II):

$$\frac{\sigma^i}{\sigma^s} \approx \frac{M}{m}\left(1-\frac{n_1\left(1-r_e\right)\left(\frac{\sigma^i}{\sigma^s}-1\right)}{\left(1-\frac{2R}{H}\eta\right)\left(\frac{\sigma^i}{\sigma^s}-1\right)+r_e}\right) \tag{28}$$

The material constants can be obtained by fitting Eq. (6) to the measured strain-stress curve in compression tests [15]. Particularly, the value of orientation factor of polycrystals, M, is 3.06, determined theoretically by Taylor [55]. Recently, this value is widely adopted in surface layer models [11, 15, 54, 56, 57], to describe flow stress of inner grains. For surface grains, the orientation factor, m, is defined as the reciprocal of Schmid factor as [10]:

$$m=\frac{1}{\cos\phi\cos\lambda} \tag{29}$$

where ϕ is the angle between normal stress and normal direction of slip plane, and λ is the angle between slip direction and normal stress. According to the Schmid law, the minimum value of m is 2, which represents the best grain orientation for lattice slip with the applied stress. Although in most surface layer models, m=2 is employed to describe the flow stress of surface grains approximately and the hybrid model is always fitted with the average stress-strain curve in experiment. But such a kind of comparison is statistically unreasonable. Since it is impossible

that all the tested samples have the same surface grain orientation, which is just the best one for deformation.

On the other hand, the scatter effect of experimental measured flow stress curve is unavoidable. And with the decrease of sample size, the scatter effect caused by the crystal anisotropy of materials becomes more significant [17]. The scaling down of specimen size makes each grain play a more significant role in plastic deformation. The lowest flow stress curve measured based on the experiments indicates that the specimen contains a largest grain size and a best grain orientation for deformation. While the highest flow stress curve represents the smallest grain size and the worst grain orientation. To describe the scatter of flow stress accurately, a new fitting procedure is employed in this study, as shown in Fig. 14.

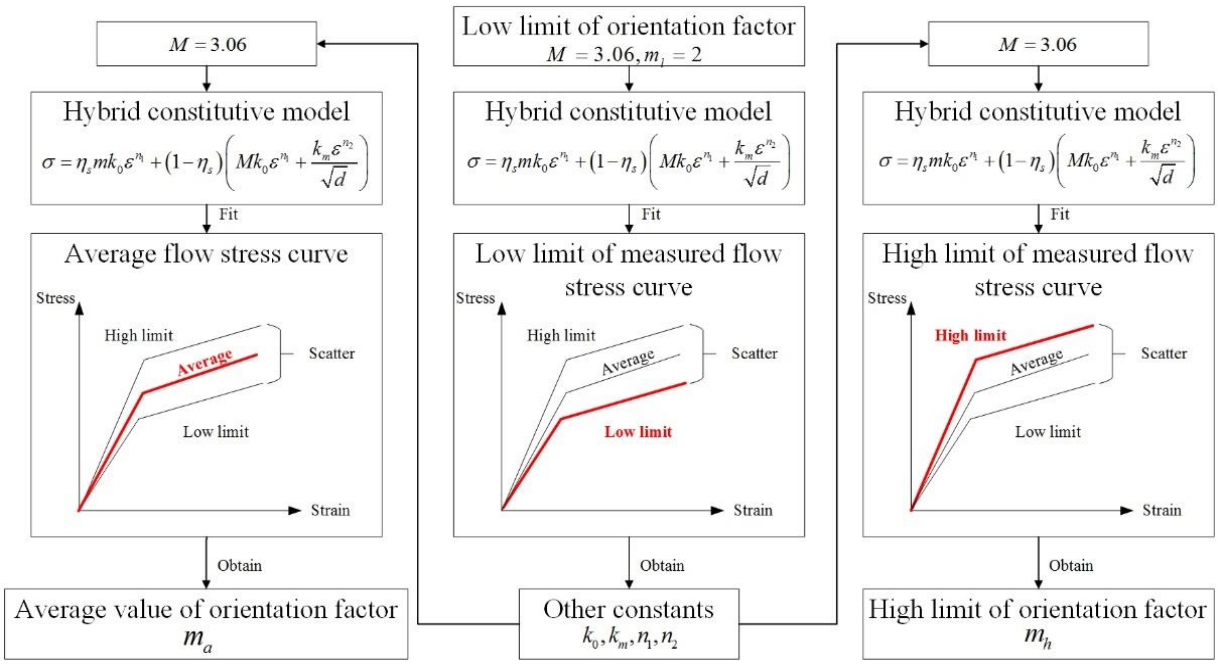


**Fig. 14.** Fitting procedure of flow stress curve

The first step in the fitting process is to determine the model parameters ($k_0$, $k_m$, $n_1$, $n_2$). The minimum value of orientation factor (M=3.06 and m=2) is adopted in this step, and the

parameters are obtained by fitting the hybrid model with the lowest flow curve measured in experiment. The second step is to determine the highest and average value of orientation factor. In this step, the model parameters obtained in the first step is used, and the orientation factor of single crystal is obtained by fitting the hybrid model with the highest and average flow curves measured in experiment respectively. The fitted curves are shown in Fig. 15, and parameters are listed in Fig. 15.

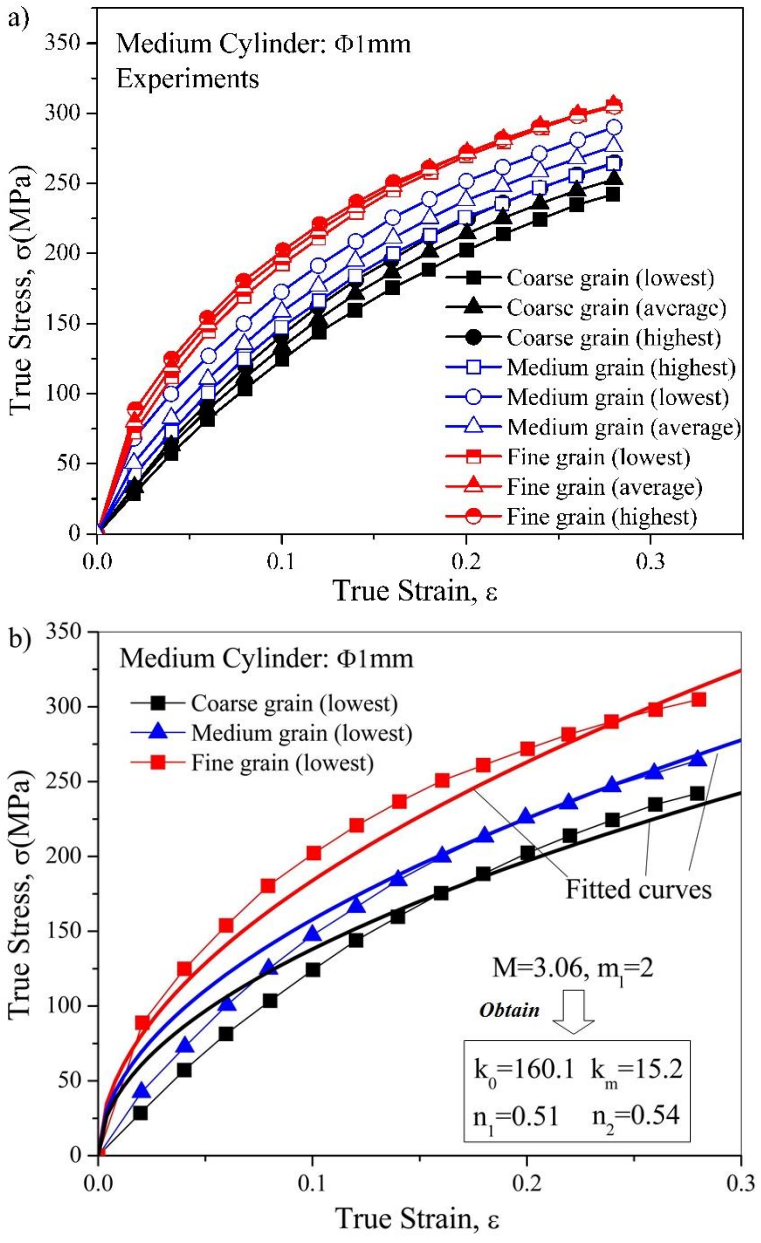

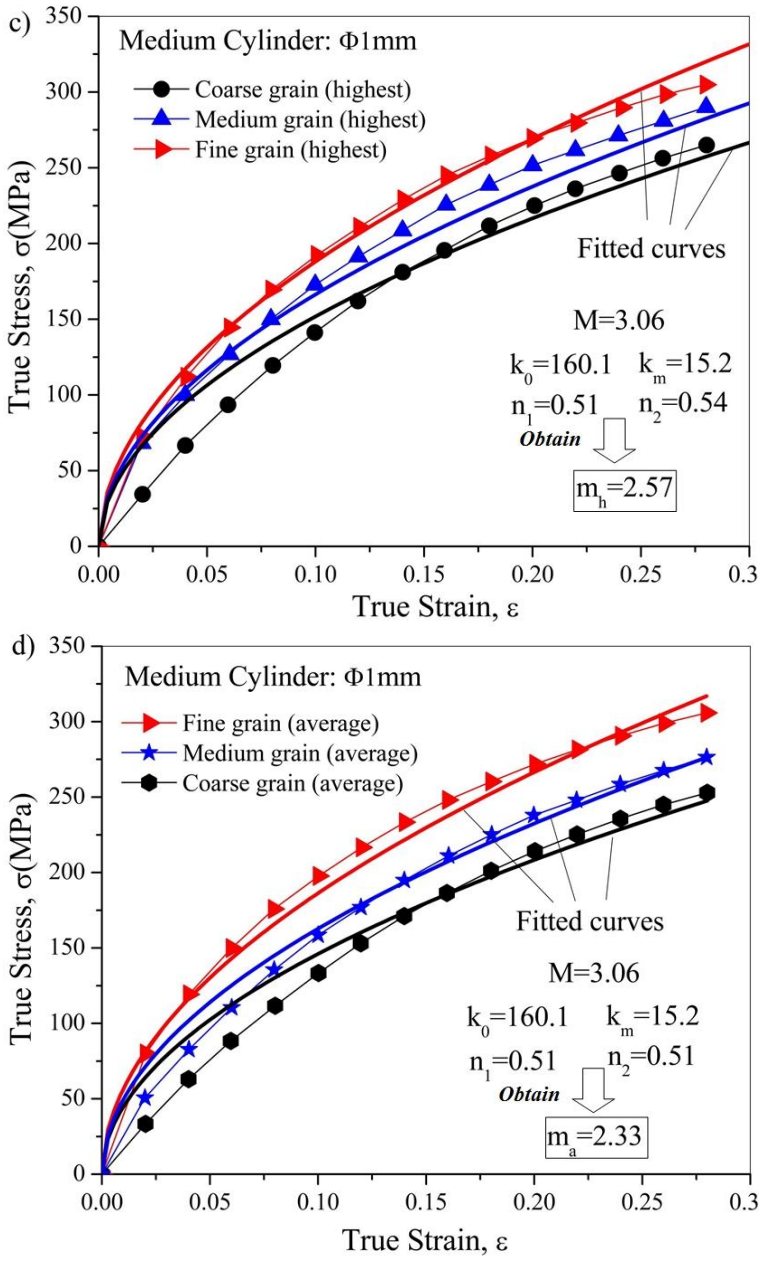


**Fig. 15.** Strain-stress curve of the medium workpieces with different grains

**Table. 2.** The parameters of the hybrid model

| Given parameters | | Fitted parameters | | | | | |
|---|---|---|---|---|---|---|---|
| $m_l$ | M | $k_0$ | $k_m$ | $n_1$ | $n_2$ | $m_h$ | $m_a$ |
| 2 | 3.06 | 160.1 | 25.2 | 0.51 | 0.54 | 2.57 | 2.33 |

By substituting these parameters into Eq. (28), the flow stress ratio can be formulated as:

$$\begin{cases} \dfrac{\sigma^i}{\sigma^s}|_l = \dfrac{M}{m_l}\left(1-\dfrac{n_1\left(1-r_e\right)\left(\dfrac{\sigma^i}{\sigma^s}|_l-1\right)}{\left(1-\dfrac{2R}{H}\eta\right)\left(\dfrac{\sigma^i}{\sigma^s}|_l-1\right)+r_e}\right)=1.53\left(1-\dfrac{0.51\left(1-r_e\right)\left(\dfrac{\sigma^i}{\sigma^s}|_l-1\right)}{\left(1-\dfrac{2R}{H}\eta\right)\left(\dfrac{\sigma^i}{\sigma^s}|_l-1\right)+r_e}\right) \\ \dfrac{\sigma^i}{\sigma^s}|_h = \dfrac{M}{m_h}\left(1-\dfrac{n_1\left(1-r_e\right)\left(\dfrac{\sigma^i}{\sigma^s}|_h-1\right)}{\left(1-\dfrac{2R}{H}\eta\right)\left(\dfrac{\sigma^i}{\sigma^s}|_h-1\right)+r_e}\right)=1.19\left(1-\dfrac{0.51\left(1-r_e\right)\left(\dfrac{\sigma^i}{\sigma^s}|_h-1\right)}{\left(1-\dfrac{2R}{H}\eta\right)\left(\dfrac{\sigma^i}{\sigma^s}|_h-1\right)+r_e}\right) \\ \dfrac{\sigma^i}{\sigma^s}|_a = \dfrac{M}{m_a}\left(1-\dfrac{n_1\left(1-r_e\right)\left(\dfrac{\sigma^i}{\sigma^s}|_a-1\right)}{\left(1-\dfrac{2R}{H}\eta\right)\left(\dfrac{\sigma^i}{\sigma^s}|_a-1\right)+r_e}\right)=1.31\left(1-\dfrac{0.51\left(1-r_e\right)\left(\dfrac{\sigma^i}{\sigma^s}|_a-1\right)}{\left(1-\dfrac{2R}{H}\eta\right)\left(\dfrac{\sigma^i}{\sigma^s}|_a-1\right)+r_e}\right) \end{cases} \quad (30)$$

where $\frac{\sigma^i}{\sigma^s}|_l \; and \; \frac{\sigma^i}{\sigma^s}|_h$ represent the lowest and highest limit of the flow stress ratio, and $\frac{\sigma^i}{\sigma^s}|_a$ is the average flow stress ratio. Solving Eq. (30), the ratio is obtained and designated as follows:

$$\begin{cases} \dfrac{\sigma^i}{\sigma^s}|_l = \dfrac{0.53r_e}{\sqrt{\left(0.25+0.22r_e+1.06\dfrac{R}{H}\eta\right)^2-2.12\left(1-\dfrac{2R}{H}\eta\right)r_e}+0.25+0.22r_e+1.06\dfrac{R}{H}\eta} \\ \dfrac{\sigma^i}{\sigma^s}|_h = \dfrac{0.19r_e}{\sqrt{\left(0.417+0.393r_e+0.38\dfrac{R}{H}\eta\right)^2-0.76\left(1-\dfrac{2R}{H}\eta\right)r_e}+0.417+0.393r_e+0.38\dfrac{R}{H}\eta} \\ \dfrac{\sigma^i}{\sigma^s}|_a = \dfrac{0.31r_e}{\sqrt{\left(0.478+0.331r_e+0.62\dfrac{R}{H}\eta\right)^2-1.24\left(1-\dfrac{2R}{H}\eta\right)r_e}+0.478+0.331r_e+0.62\dfrac{R}{H}\eta} \end{cases} \quad (31)$$

## 4.3 Numerical results

As the velocity field is assumed based on the initial shape of workpiece and the application of the model is limited to a small deformation range, the experimental results for the case with the reduction of 25% was used to validate the model. Actually, the calculated barreling parameter, b, is not a direct observation in the experiments. Ebrahimi and Najafizadeh [39] formulated an expression for representation of b based on the assumption that there is no significant barreling and the expression is given by:

$$b = 4\frac{\Delta R}{R_r}\frac{H_r}{\Delta H} \quad (32)$$

where ΔR is the difference between the maximum and top radius. $R_r$ is the average radius of the workpiece after reduction, and can be calculated using $R_r = R\sqrt{\frac{H}{H_r}}$. ΔH is the reduced height in compression. Considering Eqs. (2) and (32), the following is obtained:

$$b = \frac{2\varphi\left(1-r_e\right)^{5/2}H}{r_e R} \quad (33)$$

Fig. 16 shows the predicted average barreling parameter at compression of 25% as a function of scale factor with friction factor varying from 0.1 to 0.15. It is found that with the increase of friction factor, the barreling phenomenon increases. With the increase of size factor, the barreling parameter decreases first and then increase, and the extreme point is around $\eta^{-1}$=3, which is in accordance to the experimental observation. Moreover, it seems the interfacial friction only affects the value of barreling but not the size dependence of barreling, since all the cases with different friction factor reveals the same tendency with the increase of size factor.

The experimental and predicted upper and lower limits as well as the average value of barreling parameter at the compression of 25% with f=0.13 are presented in Fig. 17. It seems that the predicted average, upper and lower limit lines reveal the same tendency as the experimental results as a function of scale factor and fit most of the experimental results well. It indicates that the interfacial friction factor is close to 0.13 in the experiments. According to the theoretical model, the minimum value of barreling is obtained around the point of $\eta^{-1}$=3 for the reduction of 25%. It means that the strain distribution that caused by interfacial friction is the most uniform throughout the specimen at this size scale from micro- to meso-scale upon the compression of 25%.

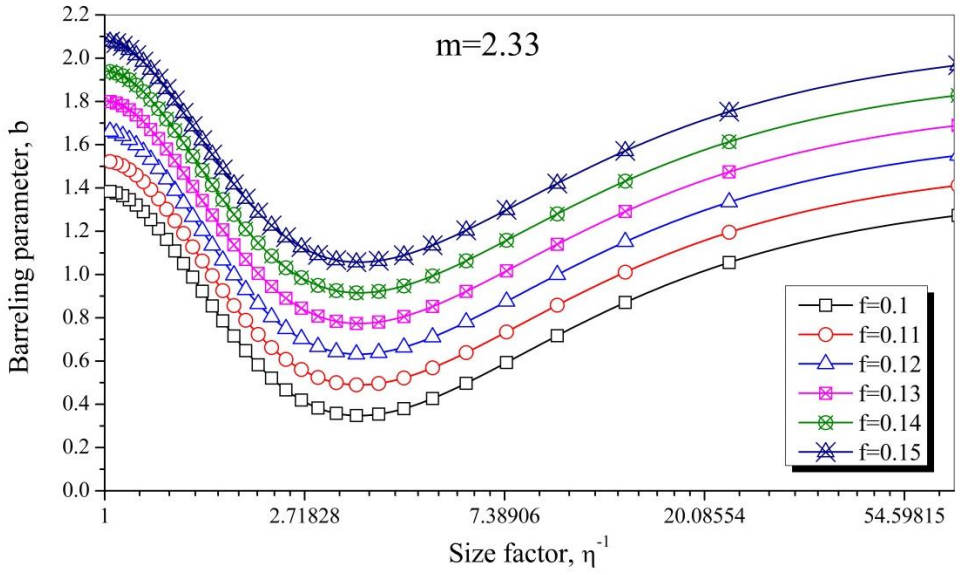


**Fig. 16.** Barreling parameter under different friction factors based on the proposed model

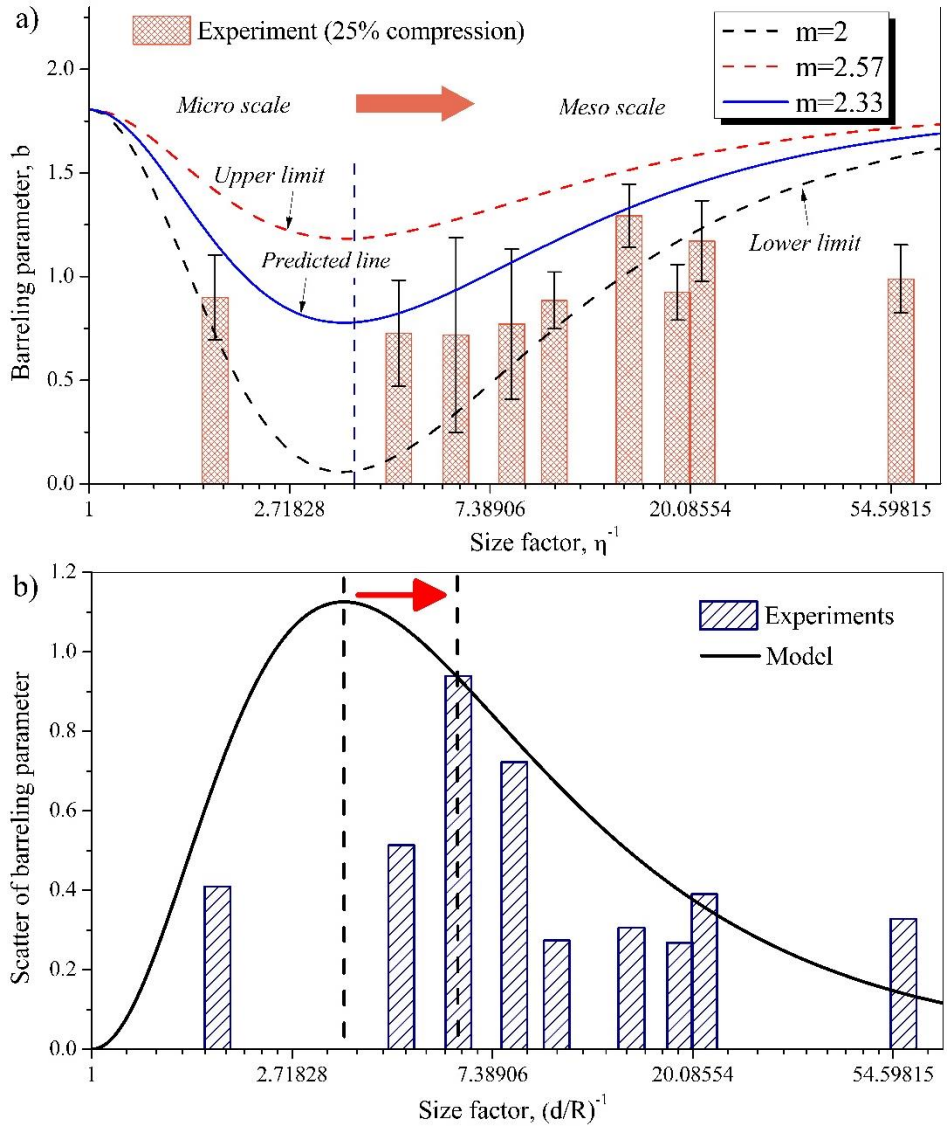


**Fig. 17.** Comparison of the experimental results and the ones based on the proposed model with f=0.13

The difference between the upper and lower limit curves in Fig. 17a) represents the scatter of barreling parameter caused by the flow stress deviation. As is the knowhow, the scatter in flow stress is caused by the crystal anisotropy, the scatter in the barreling shape is thus intrinsic. According to the proposed model, with the increase of size scale, the scatter in barreling parameter increases first and then decreases. The scale point where the scatter has the largest

value is just the same as the point with the lowest barreling parameter. It reveals that at this scale point the scatter in individual grain properties plays the most significant role in the deformation of specimen from micro- to meso-scale. There is theoretically no scatter in barreling for single crystal and macro-scaled specimens. It means the deformation of specimen is not influenced by the change of the individual grain properties at these scales. Fig. 17b) shows the comparison of the predicted and measured scatter of barreling parameter. It is found the both the scatter value and its variation with size scale are well predicted. However, the scale point of the extremum is a little different. This may be due to the experimental error in measuring the grain sizes.

## 5 Theoretical analysis and discussion

### 5.1 Dissipated energy caused by restrictions

Taking advantage of the proposed model, the dissipated energies caused by the surface and inter-grain restrictions in different scales are calculated in this section.

Generally, the dissipated energy caused by restrictions, $\dot{w}_r$, is considered by.

$$\dot{w}_r = J - \dot{w}_s \tag{34}$$

Here, J is the total deformation energy in compression process, given by eq.(21). $\dot{w}_s$ refers to the deformation energy of the specimen with all the grains free to rotate without surface friction. If the energy of grain rotation is eliminated, $\dot{w}_s$ equals to the rate of deformation work of the ideal scenario, where all the grains in the specimen are in the best grain orientation for lattice slip with the applied stress. Thus the following equation can be deduced based on Eq.(21).

$$\dot{w}_s = \frac{\pi\sigma^0 b\dot{u}}{3\sqrt{3}H}\left(\left(\frac{12H^2}{b^2}+R^2\right)^{3/2} - \left(\frac{12H^2}{b^2}\right)^{3/2}\right) \tag{35}$$

where $\sigma^0$ is the flow stress of single crystal in the best grain orientation for lattice slip with the applied stress. According to Eqs.(5) and (29), the following equation can be obtained:

$$\sigma^0 = m_l k_1 \varepsilon^{n_1} \tag{36}$$

As inter-grain restriction only applies to inner grains, the dissipated energy caused by inter-grain restriction, $\dot{w}_{ri}$, is given by:

$$\dot{w}_{ri} = \dot{w}_{Ii} - \dot{w}_{si} \tag{37}$$

where $\dot{w}_{It}$ is the deformation work of inner grains given by Eq.(19), and $\dot{w}_{si}$ is the ideal deformation work when all the inner grains are assumed in the best grain orientation of lattice slip with the applied stress. Thus, based on Eq.(19), $\dot{w}_{si}$ can be expressed as follows:

$$\dot{w}_{si} = \frac{\pi\sigma^0 b\dot{u}}{3\sqrt{3}H}\left(\left(\frac{12H^2}{b^2} + \left(R-w\right)^2\right)^{3/2} - \left(\frac{12H^2}{b^2}\right)^{3/2}\right)\frac{1-e^{(w/H-1/2)b}}{1-e^{-b/2}} \tag{38}$$

The dissipated energy caused by surface constraints can be obtained as follows:

$$\dot{w}_{re} = \dot{w}_r - \dot{w}_{ri} \tag{39}$$

The shares of the dissipated energy by surface constrictions, $R_{re}$, and inter-grain restriction, $R_{ri}$, in the total ratio of deformation work can be expressed as follows:

$$\begin{cases} R_{re} = \dfrac{\dot{w}_{re}}{J} \\ R_{ri} = \dfrac{\dot{w}_{ri}}{J} \end{cases} \tag{40}$$

By substituting Eqs.(34), (35), (36), (38) and (39) into (40), the following equation is obtained

$$\begin{cases} R_{re}=1-R_{ri}-\dfrac{\dfrac{m_l}{m_a}\left(\left(\dfrac{12H^2}{R^2b^2}+1\right)^{3/2}-\left(\dfrac{12H^2}{R^2b^2}\right)^{3/2}\right)}{\left(\dfrac{12H^2}{R^2b^2}+1\right)^{3/2}-\left(\dfrac{12H^2}{R^2b^2}\right)^{3/2}+\dfrac{\left(\eta+\dfrac{\sigma^i}{\sigma^s}(1-\eta)\right)fe^{-b/2}}{1-e^{-b/2}}+\left(\dfrac{\sigma^i}{\sigma^s}-1\right)\left(\left(\dfrac{12H^2}{R^2b^2}+(1-\eta)^2\right)^{3/2}-\left(\dfrac{12H^2}{R^2b^2}\right)^{3/2}\right)\dfrac{1-e^{(\eta R/H-1/2)b}}{1-e^{-b/2}}} \\ R_{ri}=\dfrac{\dfrac{\sigma^i}{\sigma^s}\left(1-\dfrac{m_l}{M}\right)\left(\left(\dfrac{12H^2}{R^2b^2}+(1-\eta)^2\right)^{3/2}-\left(\dfrac{12H^2}{R^2b^2}\right)^{3/2}\right)\dfrac{1-e^{(\eta R/H-1/2)b}}{1-e^{-b/2}}}{\left(\dfrac{12H^2}{R^2b^2}+1\right)^{3/2}-\left(\dfrac{12H^2}{R^2b^2}\right)^{3/2}+\dfrac{\left(\eta+\dfrac{\sigma^i}{\sigma^s}(1-\eta)\right)fe^{-b/2}}{1-e^{-b/2}}+\left(\dfrac{\sigma^i}{\sigma^s}-1\right)\left(\left(\dfrac{12H^2}{R^2b^2}+(1-\eta)^2\right)^{3/2}-\left(\dfrac{12H^2}{R^2b^2}\right)^{3/2}\right)\dfrac{1-e^{(\eta R/H-1/2)b}}{1-e^{-b/2}}} \end{cases} \quad (41)$$

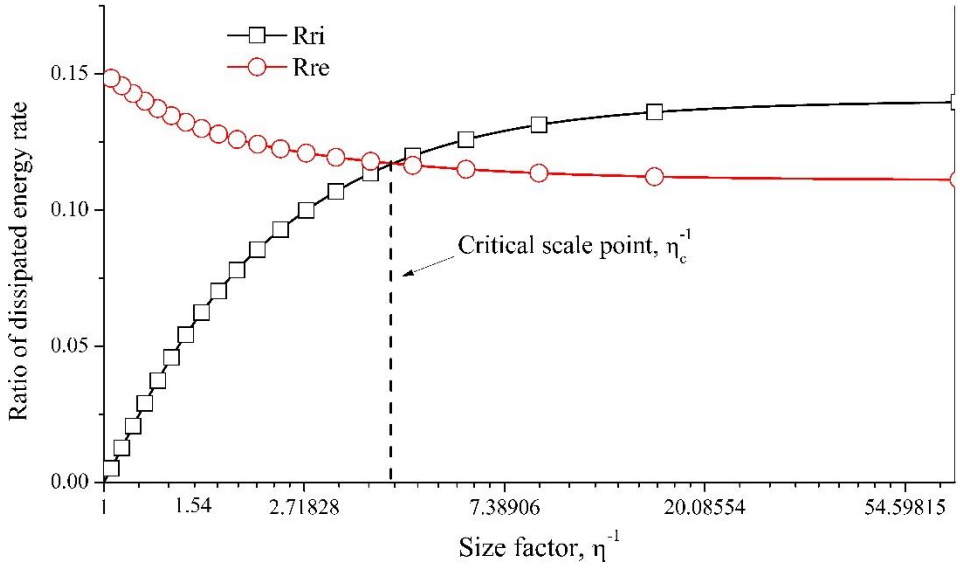


**Fig. 18.** The shares of dissipated energy rate caused by external restriction and inter-grain restriction in the total deformation energy rate as a function of scale factor

Taking the parameters listed in Table. 2, $R_{re}$ and $R_{ri}$ can be calculated. Fig. 18 shows the evolution of $R_{re}$ and $R_{ri}$ with the change of size scales. Obviously, $R_{re}$ decreases with the increase of scale factor. It means the influence of surface constraints on the overall deformation become less significant in macro scale than in micro scale specimen. However, the influence of inter-grain restriction is more significant in larger scale, because $R_{ri}$ increases with scale factor. A critical scale point, $\eta_c^{-1}=4$, can be obtained at the cross point of the lines in Fig. 18.

Generally, when the scale factor is smaller than $\eta_c^{-1}$, $R_{re} > R_{ri}$, and when the scale factor is larger than , $\eta_c^{-1}$, $R_{re} < R_{ri}$. It indicates that the dominating restriction in forming process changes with size scale. In micro scale, surface constraints is dominating. However, in the macro scale, the dominating restriction changes into inter-grain restriction. It is accordance to the experimental observations mentioned above, and it further explains the reason of the difference in the distribution of deformation bands with the decrease of size scale.

Based on the experimental observations and the theoretical analysis, the co-effect of microstructure and external constraints on plastic deformation in micro- and meso- scale forming process can be obtained as shown in Fig. 19. Based on the value of R/d, the size scale can be divided into two parts. When scale factor R/d is smaller than 4, the size effect on plastic deformation is mainly induced by the external constraints. The dominating mechanism of size effect in this period of scale is the share of interface decreases with the increase of specimen size. When scale factor R/d is larger than 4, microstructure size effect becoming more important than interface. And the dominating mechanism is the increase share of inner grains with the increase of specimen size.

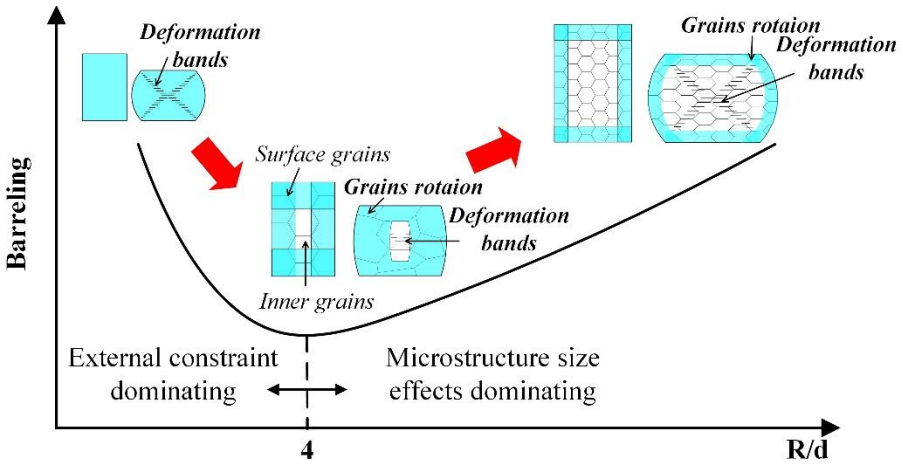

**Fig. 19.** Co-effect of microstructure and external constraints on plastic deformation in micro- and meso scale forming process

## 6 Conclusions

The co-effect of microstructure and surface constraints on plastic deformation in the micro- and meso-scaled forming process was studied by barreling compression experiments and analytical modeling. The following concluding remarks can be drawn accordingly.

1. The barreling compression tests showed that the barreling shape in compression process is affected by the scale factor η. With the decrease of η from 1 to 0.05, the significance of barreling firstly decreases to an extremal point and then increases.

2. The mechanism of the size effect on barreling in compression process is found to be the transformation of dominating restriction to grain rotation from inter-grain restriction to surface constraints, with the decrease of size scale. By considering both of the constraints, an extended upper-bound solution of barreling considering surface layer model was established. The comparison between the theoretical analysis and experiments also validates the mechanism of size effect.

3. The size effect on plastic deformation induced by the co-effect of microstructure and surface constraints takes place when there are 8 grains in diameter of the cylinder, if the ratio of diameter to height is 2/3. When there are fewer grains in the diameter, surface constraints dissipate more energy than inter-grain restrictions, and the size effect mainly induced by surface constraints. When there are more than 8 grains inter-grain restrictions dissipate more energy, and microstructure become the source of size effect.

**Acknowledgments**

This work was supported by the General Research Fund of National Natural Science Foundation of China (No. 51522506, No. 51421092 and No. 51575465), the Hong Kong GRF project of 152792/16E and the project of G-SB91 from The Hong Kong Polytechnic University.

**References**

[1] M. Geiger, M. Kleiner, R. Eckstein, N. Tiesler, U. Engel, Microforming, CIRP Annals - Manufacturing Technology, 50 (2001) 445-462.
[2] U. Engel, R. Eckstein, Microforming—from basic research to its realization, Journal of Materials Processing Technology, 125–126 (2002) 35-44.
[3] M.W. Fu, J.L. Wang, A.M. Korsunsky, A review of geometrical and microstructural size effects in micro-scale deformation processing of metallic alloy components, International Journal of Machine Tools and Manufacture, 109 (2016) 94-125.
[4] Y.J. Deng, L.F. Peng, X.M. Lai, M.W. Fu, Z.Q. Lin, Constitutive modeling of size effect on deformation behaviors of amorphous polymers in micro-scaled deformation, International Journal of Plasticity, 89 (2017) 197-222.
[5] F. Vollertsen, H. Schulze Niehoff, Z. Hu, State of the art in micro forming, International Journal of Machine Tools and Manufacture, 46 (2006) 1172-1179.
[6] B. Eichenhueller, E. Egerer, U. Engel, Microforming at elevated temperature - forming and material behaviour, The International Journal of Advanced Manufacturing Technology, 33 (2007) 119-124.
[7] M.W. Fu, W.L. Chan, A review on the state-of-the-art microforming technologies, The International Journal of Advanced Manufacturing Technology, 67 (2013) 2411-2437.
[8] G.-Y. Kim, J. Ni, M. Koç, Modeling of the Size Effects on the Behavior of Metals in Microscale Deformation Processes, Journal of Manufacturing Science and Engineering, 129 (2006) 470-476.
[9] N. Krishnan, J. Cao, K. Dohda, Study of the Size Effect on Friction Conditions in Microextrusion—Part I: Microextrusion Experiments and Analysis, Journal of Manufacturing Science and Engineering, 129 (2006) 669-676.
[10] X.M. Lai, L.F. Peng, P. Hu, S.H. Lan, J. Ni, Material behavior modelling in micro/meso-scale forming process with considering size/scale effects, Computational Materials Science, 43 (2008) 1003-1009.
[11] L.F. Peng, X.M. Lai, H.-J. Lee, J.-H. Song, J. Ni, Analysis of micro/mesoscale sheet forming process with uniform size dependent material constitutive model, Materials Science and Engineering: A, 526 (2009) 93-99.
[12] W.L. Chan, M.W. Fu, J. Lu, J.G. Liu, Modeling of grain size effect on micro deformation behavior in micro-forming of pure copper, Materials Science and Engineering: A, 527 (2010) 6638-6648.
[13] M. Klein, A. Hadrboletz, B. Weiss, G. Khatibi, The 'size effect' on the stress–strain, fatigue and fracture properties of thin metallic foils, Materials Science and Engineering: A, 319 (2001) 924-928.

[14] N. Hansen, The effect of grain size and strain on the tensile flow stress of aluminium at room temperature, Acta Metallurgica, 25 (1977) 863-869.
[15] Z.T. Xu, L.F. Peng, M.W. Fu, X.M. Lai, Size effect affected formability of sheet metals in micro/meso scale plastic deformation: Experiment and modeling, International Journal of Plasticity, 68 (2015) 34-54.
[16] T. Furushima, H. Tsunezaki, K.-i. Manabe, S. Alexsandrov, Ductile fracture and free surface roughening behaviors of pure copper foils for micro/meso-scale forming, International Journal of Machine Tools and Manufacture, 76 (2014) 34-48.
[17] W.L. Chan, M.W. Fu, J. Lu, The size effect on micro deformation behaviour in micro-scale plastic deformation, Materials & design, 32 (2011) 198-206.
[18] W.L. Chan, M.W. Fu, B. Yang, Experimental studies of the size effect affected microscale plastic deformation in micro upsetting process, Materials Science and Engineering: A, 534 (2012) 374-383.
[19] J.S. Stölken, A.G. Evans, A microbend test method for measuring the plasticity length scale, Acta Materialia, 46 (1998) 5109-5115.
[20] M.G.D. Geers, W.A.M. Brekelmans, P.J.M. Janssen, Size effects in miniaturized polycrystalline FCC samples: Strengthening versus weakening, International Journal of Solids and Structures, 43 (2006) 7304-7321.
[21] N.A. Fleck, G.M. Muller, M.F. Ashby, J.W. Hutchinson, Strain gradient plasticity: Theory and experiment, Acta Metallurgica et Materialia, 42 (1994) 475-487.
[22] A.A. Elmustafa, J.A. Eastman, M.N. Rittner, J.R. Weertman, D.S. Stone, Indentation size effect: large grained aluminum versus nanocrystalline aluminum-zirconium alloys, Scripta Materialia, 43 (2000) 951-955.
[23] J.R. Greer, W.C. Oliver, W.D. Nix, Size dependence of mechanical properties of gold at the micron scale in the absence of strain gradients, Acta Materialia, 53 (2005) 1821-1830.
[24] T.A. Kals, R. Eckstein, Miniaturization in sheet metal working, Journal of Materials Processing Technology, 103 (2000) 95-101.
[25] E. Arzt, Size effects in materials due to microstructural and dimensional constraints: a comparative review, Acta Materialia, 46 (1998) 5611-5626.
[26] J.G. Liu, M.W. Fu, J. Lu, W.L. Chan, Influence of size effect on the springback of sheet metal foils in micro-bending, Computational Materials Science, 50 (2011) 2604-2614.
[27] J.-T. Gau, C. Principe, M. Yu, Springback behavior of brass in micro sheet forming, Journal of Materials Processing Technology, 191 (2007) 7-10.
[28] A. Diehl, U. Engel, M. Geiger, Influence of microstructure on the mechanical properties and the forming behaviour of very thin metal foils, The International Journal of Advanced Manufacturing Technology, 47 (2010) 53-61.
[29] S.Y. Lin, F.C. Lin, Prediction of fold defect in barreling formations of cylinder upsetting, Finite Elements in Analysis and Design, 39 (2003) 325-341.
[30] K. Kulkarni, S. Kalpakjian, A study of barreling as an example of free deformation in plastic working, Journal of Engineering for Industry, 91 (1969) 743-754.
[31] B. Avitzur, R. Kohser, Disk and Strip Forging with Side-surface Foldover—Part 1: Velocity Field and Upper-Bound Analysis, Journal of Engineering for Industry, 100 (1978) 421-427.
[32] K. Manisekar, R. Narayanasamy, S. Malayappan, Effect of friction on barrelling in square billets of aluminium during cold upset forging, Materials & design, 27 (2006) 147-155.

[33] R. Narayanasamy, S. Sathiyanarayanan, R. Ponalagusamy, A study on barrelling in magnesium alloy solid cylinders during cold upset forming, Journal of Materials Processing Technology, 101 (2000) 64-69.
[34] A.H. Shabaik, Prediction of the geometry changes of the free boundary during upsetting by the slip-line theory, Journal of Engineering for Industry, 93 (1971) 586-592.
[35] W. Schroeder, D. Webster, Press-forging thin sections-effect of friction, are, and thickness on pressures requied, Journal of applied mechanics-transactions of the ASME, 16 (1949) 289-294.
[36] S. Kobayashi, Upper-bound solutions of axisymmetric forming problems—I, Journal of Engineering for Industry, 86 (1964) 122-126.
[37] S. Kobayashi, Upper-bound solutions of axisymmetric forming problems—II, Journal of Engineering for Industry, 86 (1964) 326-332.
[38] B. Avitzur, Metal forming: Processes and analysis, Mcgraw-hill, INC., New York. 1968, 500 P, (1968).
[39] R. Ebrahimi, A. Najafizadeh, A new method for evaluation of friction in bulk metal forming, Journal of Materials Processing Technology, 152 (2004) 136-143.
[40] Y. Li, E. Onodera, A. Chiba, Evaluation of friction coefficient by simulation in bulk metal forming process, Metallurgical and Materials Transactions A, 41 (2010) 224-232.
[41] Z. Yao, D. Mei, H. Shen, Z. Chen, A friction evaluation method based on barrel compression test, Tribology Letters, 51 (2013) 525-535.
[42] P. Sivaprasad, C. Davies, An assessment of the interface friction factor using the geometry of upset specimens, Modelling and Simulation in Materials Science and Engineering, 13 (2005) 355.
[43] A.K. Kaviti, O. Prakash, P. Vishwanath, Friction calibration map for determination of equal frictional conditions, Adv. Appl. Sci. Res, 2 (2011) 279-289.
[44] C.J. Wang, C.J. Wang, J. Xu, P. Zhang, D.B. Shan, B. Guo, Plastic deformation size effects in micro-compression of pure nickel with a few grains across diameter, Materials Science and Engineering: A, 636 (2015) 352-360.
[45] S.R. Kalidindi, S.E. Schoenfeld, On the prediction of yield surfaces by the crystal plasticity models for fcc polycrystals, Materials Science and Engineering: A, 293 (2000) 120-129.
[46] Z. Zhao, M. Ramesh, D. Raabe, A.M. Cuitiño, R. Radovitzky, Investigation of three-dimensional aspects of grain-scale plastic surface deformation of an aluminum oligocrystal, International Journal of Plasticity, 24 (2008) 2278-2297.
[47] I. Tikhovskiy, D. Raabe, F. Roters, Simulation of earing during deep drawing of an Al–3% Mg alloy (AA 5754) using a texture component crystal plasticity FEM, Journal of Materials Processing Technology, 183 (2007) 169-175.
[48] F. Roters, P. Eisenlohr, L. Hantcherli, D.D. Tjahjanto, T.R. Bieler, D. Raabe, Overview of constitutive laws, kinematics, homogenization and multiscale methods in crystal plasticity finite-element modeling: Theory, experiments, applications, Acta Materialia, 58 (2010) 1152-1211.
[49] J. Banerjee, Barreling of solid cylinders under axial compression, Journal of Engineering Materials and Technology, 107 (1985) 138-144.
[50] K. Higashida, J. Takamura, N. Narita, The formation of deformation bands in f.c.c. crystals, Materials Science and Engineering, 81 (1986) 239-258.
[51] N. Hansen, Polycrystalline strengthening, Metallurgical Transactions A, 16 (1985) 2167-2190.

[52] B. Clausen, T. Lorentzen, T. Leffers, Self-consistent modelling of the plastic deformation of f.c.c. polycrystals and its implications for diffraction measurements of internal stresses, Acta Materialia, 46 (1998) 3087-3098.
[53] H. Mecking, U.F. Kocks, Kinetics of flow and strain-hardening, Acta Metallurgica, 29 (1981) 1865-1875.
[54] J.Q. Ran, M.W. Fu, W.L. Chan, The influence of size effect on the ductile fracture in micro-scaled plastic deformation, International Journal of Plasticity, 41 (2013) 65-81.
[55] G.I. Taylor, H. Quinney, The Plastic Distortion of Metals, Philosophical Transactions of the Royal Society of London. Series A, Containing Papers of a Mathematical or Physical Character, 230 (1932) 323-362.
[56] C. Keller, E. Hug, A.M. Habraken, L. Duchene, Finite element analysis of the free surface effects on the mechanical behavior of thin nickel polycrystals, International Journal of Plasticity, 29 (2012) 155-172.
[57] J.Q. Ran, M.W. Fu, A hybrid model for analysis of ductile fracture in micro-scaled plastic deformation of multiphase alloys, International Journal of Plasticity, 61 (2014) 1-16.

# Appendix I

Eq. (23) can be further written as:

$$\frac{p_{ave}}{\sigma}=\frac{R}{3\sqrt{3}b^2H\left(1+\left(\frac{\sigma^i}{\sigma^s}-1\right)(1-\eta)^2\left(1-\frac{2R}{H}\eta\right)\right)}\left(\begin{array}{l}\left(\frac{12H^2}{R^2}+b^2\right)^{3/2}-\left(\frac{12H^2}{R^2}\right)^{3/2}+\frac{\left(1+\left(\frac{\sigma^i}{\sigma^s}-1\right)(1-\eta)^2\left(1-\frac{2R}{H}\eta\right)\right)b^3fe^{-b/2}}{1-e^{-b/2}}\\+\left(\frac{\sigma^i}{\sigma^s}-1\right)\left(\left(\frac{12H^2}{R^2}+b^2(1-\eta)^2\right)^{3/2}-\left(\frac{12H^2}{R^2}\right)^{3/2}\right)\frac{1-e^{(\eta R/H-1/2)b}}{1-e^{-b/2}}\end{array}\right)$$

$$=\frac{R}{3\sqrt{3}H\left(1+\left(\frac{\sigma^i}{\sigma^s}-1\right)(1-\eta)^2\left(1-\frac{2R}{H}\eta\right)\right)}\left(\begin{array}{l}\frac{1}{b^2}\left(\left(\frac{12H^2}{R^2}+b^2\right)^{3/2}-\left(\frac{12H^2}{R^2}\right)^{3/2}\right)+\frac{be^{-b/2}}{1-e^{-b/2}}\left(1+\left(\frac{\sigma^i}{\sigma^s}-1\right)(1-\eta)^2\left(1-\frac{2R}{H}\eta\right)\right)f\\+\left(\frac{\sigma^i}{\sigma^s}-1\right)\frac{1}{b^2}\left(\left(\frac{12H^2}{R^2}+b^2(1-\eta)^2\right)^{3/2}-\left(\frac{12H^2}{R^2}\right)^{3/2}\right)\frac{1-e^{(\eta R/H-1/2)b}}{1-e^{-b/2}}\end{array}\right)$$

$$=\frac{1}{3\sqrt{3}}\frac{R}{H\eta_v}\left(P_1+\eta_v fP_2+\eta_s P_3\right)$$

(a1)

And the parameters are given by

$$\begin{aligned}P_1&=\frac{1}{b^2}\left(\frac{12H^2}{R^2}\right)^{3/2}\left(\left(1+\frac{b^2R^2}{12H^2}\right)^{3/2}-1\right)\\P_2&=\frac{be^{-b/2}}{1-e^{-b/2}}\\P_3&=\frac{1}{b^2}\left(\frac{12H^2}{R^2}\right)^{3/2}\left(\left(1+\frac{b^2R^2}{12H^2}(1-\eta)^2\right)^{3/2}-1\right)\frac{1-e^{(\eta R/H-1/2)b}}{1-e^{-b/2}}\\\eta_v&=1+\left(\frac{\sigma^i}{\sigma^s}-1\right)(1-\eta)^2\left(1-\frac{2R}{H}\eta\right)\\\eta_s&=\frac{\sigma^i}{\sigma^s}-1\end{aligned}$$

(a2)

According to the upper boundary theory in the following

$$\frac{\partial\left(\frac{p_{ave}}{\sigma}\right)}{\partial b}=0$$

(a3)

The following equation is thus obtained

$$\frac{\partial P_1}{\partial b}+\eta_v f\frac{\partial P_2}{\partial b}+\eta_s\frac{\partial P_3}{\partial b}=0 \tag{a4}$$

For cylinders with a larger height than the diameter, the term $\frac{b^2R^2}{12H^2}<\frac{b^2}{48}\ll 1$. Similarly, $\frac{b^2R^2}{12H^2}(1-\eta)^2\ll 1$ is also obtained, since $\eta<1$. Thus the approximation can be deduced using Taylor expansion and ignoring the small terms.

$$\begin{aligned}\left(1+\frac{b^2R^2}{12H^2}\right)^{3/2}&\approx 1+\frac{b^2R^2}{8H^2}+\frac{3}{8}\left(\frac{b^2R^2}{12H^2}\right)^2\\ \left(1+\frac{b^2R^2}{12H^2}(1-\eta)^2\right)^{3/2}&\approx 1+\frac{b^2R^2}{8H^2}(1-\eta)^2+\frac{3}{8}\left(\frac{b^2R^2}{12H^2}(1-\eta)^2\right)^2\end{aligned} \tag{a5}$$

Similarly, the terms of exponential functions can also expanded using Taylor series. And considering the condition that $\left|\eta\frac{R}{H}b\right|<\left|-\frac{1}{2}b\right|<1$, the exponential terms can be approximated by

$$\begin{aligned}e^{b\eta R/H}&=\sum_{n=0}^{\infty}\frac{(b\eta R/H)^n}{n!}\approx 1+b\eta R/H\\ e^{-b/2}&=\sum_{n=0}^{\infty}\frac{\left[-\frac{b}{2}\right]^n}{n!}\approx 1-\frac{b}{2}\end{aligned} \tag{a6}$$

Substituting Eqs. (a5) (a6) into Eq. (a1), the following equation is obtained:

$$\begin{aligned}P_1&=\frac{1}{b^2}\left(\frac{12H^2}{R^2}\right)^{3/2}\left(\frac{b^2R^2}{8H^2}+\frac{3}{8}\left(\frac{b^2R^2}{12H^2}\right)^2\right)\\ P_2&=\frac{be^{-b/2}}{1-e^{-b/2}}\approx 2-b\\ P_3&=\frac{1}{b^2}\left(\frac{12H^2}{R^2}\right)^{3/2}\left(\frac{b^2R^2}{8H^2}(1-\eta)^2+\frac{3}{8}\left(\frac{b^2R^2}{12H^2}(1-\eta)^2\right)^2\right)\frac{1-e^{(\eta R/H-1/2)b}}{1-e^{-b/2}}\end{aligned} \tag{a7}$$

Thus their partial derivatives are established as follows

$$\frac{\partial P_1}{\partial b}=\frac{\sqrt{3}R}{8H}b$$

$$\frac{\partial P_2}{\partial b}=-1$$

$$\frac{\partial P_3}{\partial b}=\left(\frac{12H^2}{R^2}\right)^{3/2}\left(1-\frac{w}{R}\right)^2\left[\begin{array}{l}\left(\frac{3}{4}\left(\frac{R^2}{12H^2}\right)^2\left(1-\frac{w}{R}\right)^2 b\right)\frac{1-e^{(w/H-1/2)b}}{1-e^{-b/2}}+\\ \left(\frac{R^2}{8H^2}+\frac{3}{8}\left(\frac{R^2}{12H^2}\right)^2\left(1-\frac{w}{R}\right)^2 b^2\right)\left(\frac{\left(\frac{1}{2}-\frac{w}{H}\right)e^{(w/H-1/2)b}}{1-e^{-b/2}}-\frac{\left(1-e^{(w/H-1/2)b}\right)e^{-b/2}}{2\left(1-e^{-b/2}\right)^2}\right)\end{array}\right]$$

$$\approx\left(1-\frac{w}{R}\right)^2\left(1-\frac{2w}{H}\right)\left(\frac{\sqrt{3}R}{8H}\left(1-\frac{w}{R}\right)^2 b+\frac{3\sqrt{3}w}{R}+\frac{\sqrt{3}Rw}{16H^2}\left(1-\frac{w}{R}\right)^2 b^2\right)$$

(a8)

Substituting Eqs. (a7) and (a8) into Eq. (a4), the following relation is generated:

$$Ab^2+Bb+C=0 \tag{a9}$$

$$\begin{aligned}A&=\frac{\sqrt{3}}{16}\eta_s\frac{R^2}{H^2}\frac{w}{R}\left(1-\frac{w}{R}\right)^4\left(1-\frac{w}{H/2}\right)\\ B&=\frac{\sqrt{3}}{8}\frac{R}{H}\left(\eta_s\left(1-\frac{w}{R}\right)^4\left(1-\frac{w}{H/2}\right)+1\right)\\ C&=\eta_s\left(1-\frac{w}{R}\right)^2\left(1-\frac{w}{H/2}\right)\left(\frac{3\sqrt{3}w}{R}-f\right)-f\end{aligned} \tag{a10}$$

Solving the above equation, the optimized barreling parameter is obtained as follows:

$$b_{opt}=\frac{-B+\sqrt{B^2-4AC}}{2A}=\frac{f-3\sqrt{3}D_1}{\frac{\sqrt{3}}{8}\frac{R}{H}\left(D_3+\sqrt{D_3-\frac{16\sqrt{3}}{3}D_2\left(f-3\sqrt{3}D_1\right)}\right)} \tag{a11}$$

$$D_1 = \frac{\eta_s \eta (1-\eta)^2 \left(1 - \frac{\eta R}{H/2}\right)}{1 + \eta_s (1-\eta)^2 \left(1 - \frac{\eta R}{H/2}\right)}$$

$$D_2 = (1-\eta)^2 D_1 \qquad \text{(a12)}$$

$$D_3 = \frac{1 + \eta_s (1-\eta)^4 \left(1 - \frac{\eta R}{H/2}\right)}{1 + \eta_s (1-\eta)^2 \left(1 - \frac{\eta R}{H/2}\right)}$$

# Appendix II

The axes are chosen and shown in Fig. 13. Assuming that the deformation is small and no significant barrel occurs on the profile of the workpiece, the y-axial force equilibrium on the interface of inner and surface grains is given by:

$$\sigma^i S^i = \sigma^s S^s \tag{b1}$$

where $S^i$ and $S^s$ are the areas at inner and surface grain sides, respectively. Due to the volume constancy, the areas can be expressed as:

$$\begin{aligned} S^i &= \frac{S_0}{1+\varepsilon_{yi}} \\ S^s &= \frac{S_0}{1+\varepsilon_{ys}} \end{aligned} \tag{b2}$$

where $\varepsilon_{yi}$ and $\varepsilon_{ys}$ are the y-axial strain of inner and surface grains. $S_0$ is the initial area of interface. Substituting Eq.(b2) into Eq.(b1), the following relation is obtained:

$$\frac{\sigma^i}{\sigma^s} = \frac{1+\varepsilon_{yi}}{1+\varepsilon_{ys}} \tag{b3}$$

The compression reduction of the workpiece is given as:

$$r_e = \frac{\Delta H}{H} = \frac{\Delta H_i + \Delta H_s}{H} = \frac{H_i\left(1-e^{\varepsilon_{yi}}\right)+H_s\left(1-e^{\varepsilon_{ys}}\right)}{H} = 1-\left(\frac{H_i}{H}e^{\varepsilon_{yi}}+\frac{H_s}{H}e^{\varepsilon_{ys}}\right) = 1-\left(\left(1-\frac{2R}{H}\eta\right)e^{\varepsilon_{yi}}+\frac{2R}{H}\eta e^{\varepsilon_{ys}}\right) \tag{b4}$$

where $H_i$, $H_s$, $\Delta H_i$ and $\Delta H_s$ are the original and reduced heights of the inner and surface grains. As the deformation is small, Eq. (b4) can be further formulated according to Taylor expansion.

$$r_e = 1-\left(\left(1-\frac{2R}{H}\eta\right)\left(1+\varepsilon_{yi}\right)+\frac{2R}{H}\eta\left(1+\varepsilon_{ys}\right)\right) \tag{b5}$$

Substituting Eq. (b3) into Eq.(b5), the following expression is given:

$$\begin{aligned}\varepsilon_{ys} &= \frac{1-r_e}{\left(1-\frac{2R}{H}\eta\right)\frac{\sigma^i}{\sigma^s}+\frac{2R}{H}\eta}-1 \\ \varepsilon_{yi} &= \frac{1-r_e}{1-\frac{2R}{H}\eta+\frac{2R}{H}\frac{\sigma^s}{\sigma^i}\eta}-1\end{aligned} \tag{b6}$$

As no barreling is assumed, the distribution of the strain in the surface and inner grains is unique, thus

$$\frac{\varepsilon_i}{\varepsilon_s}\approx\frac{\varepsilon_{yi}}{\varepsilon_{ys}}=\frac{\frac{1-r_e}{1-\frac{2R}{H}\eta+\frac{2R}{H}\frac{\sigma^s}{\sigma^i}\eta}-1}{\frac{1-r_e}{\left(1-\frac{2R}{H}\eta\right)\frac{\sigma^i}{\sigma^s}+\frac{2R}{H}\eta}-1}=\frac{\left(1-\frac{2R}{H}\eta\right)\frac{\sigma^i}{\sigma^s}+\frac{2R}{H}\eta-\left(1-r_e\right)\frac{\sigma^i}{\sigma^s}}{\left(1-\frac{2R}{H}\eta\right)\frac{\sigma^i}{\sigma^s}+\frac{2R}{H}\eta-\left(1-r_e\right)}=1-\frac{\left(1-r_e\right)\left(\frac{\sigma^i}{\sigma^s}-1\right)}{\left(1-\frac{2R}{H}\eta\right)\left(\frac{\sigma^i}{\sigma^s}-1\right)+r_e} \tag{b7}$$

Substituting Eq.(b7) into Eq.(27), the following expression is obtained:

$$\frac{\sigma^i}{\sigma^s}=\frac{M}{m}\left(1+\frac{k_m\varepsilon_{inner}^{\ n_2-n_1}}{M\sqrt{d}k_0}\right)\left(1-\frac{\left(1-r_e\right)\left(\frac{\sigma^i}{\sigma^s}-1\right)}{\left(1-\frac{2R}{H}\eta\right)\left(\frac{\sigma^i}{\sigma^s}-1\right)+r_e}\right)^{n_1} \tag{b8}$$

where r is the compression reduction of the workpiece. Considering that the surface grains are much easier to be deformed than inner grains, most deformation is distributed in the surface grains with small r, thus $\varepsilon_{inner}\approx 0$. If $r > \frac{2R}{H}\eta\left(1-\frac{\sigma^s}{\sigma^i}\right)$, $\left|\frac{(1-r_e)\left(\frac{\sigma^i}{\sigma^s}-1\right)}{\left(1-\frac{2R}{H}\eta\right)\left(\frac{\sigma^i}{\sigma^s}-1\right)-r_e}\right|<1$. In tandem with Taylor expansion, Eq. (b8) is approximated to

$$\frac{\sigma^i}{\sigma^s} \approx \frac{M}{m}\left(1-\frac{n_1\left(1-r_e\right)\left(\frac{\sigma^i}{\sigma^s}-1\right)}{\left(1-\frac{2R}{H}\eta\right)\left(\frac{\sigma^i}{\sigma^s}-1\right)+r_e}\right) \tag{b9}$$